**Mineral Compositions as Governed by Spin-spin Interactions: Evidence for a Compositionally Layered, Inhomogeneous Mantle**

A Thesis Submitted to the College of

Graduate Studies and Research

In Partial Fulfillment of the Requirements

For the Degree of Master's of Science

In the Department of Geological Sciences

University of Saskatchewan

Saskatoon

By Jacques K. Desmarais

Permission to Use

In presenting this thesis in partial fulfilment of the requirements for a postgraduate degree from the University of Saskatchewan, I agree that the libraries of this university may make it freely available for inspection. I further agree that permission for copying of this thesis in any manner, in whole or in part, for scholarly purposes may be granted by the professor who supervised my thesis work or, in their absence, by the Head of the Department of Geological Sciences or the Dean of the College of Graduate Studies and Research. It is understood that any copying or publication or use of this thesis or parts thereof for financial gain shall not be allowed without my written permission. It is also understood that due recognition shall be given to me and to the University of Saskatchewan in any scholarly use which may be made of any materials in my thesis.

Requests for permission to copy or to make other use of material in this thesis in whole or part should be addressed to:

Head of the Department of Geological Sciences

114 Science Place

University of Saskatchewan

Saskatoon, Saskatchewan

Canada

S7N 5E2

**Abstract**

The hypothesis that the Earth's mantle is composed of chemically distinct layers has long provided a solution to reconcile chemical differences between mid-ocean ridge basalts and ocean-island basalts. In particular, a perovskitic lower mantle can account for the "missing silicon problem", whereby the upper mantle Mg/Si ratios are systematically higher than chondritic values. Knowledge of the bulk chemical and mineralogical profile of the mantle is crucial in constraining models of Earth's convection and dynamics in time, which controls the evolution of igneous processes over Earth's history. The main argument against compositional layering in Earth's mantle has been observations from seismic waves that subducted slabs reach the lower mantle, which imply the existence of a component of whole mantle convection. However, recent geodynamical modeling has shown that subducted slabs can reach the lower mantle in models including chemical layering. Here, we provide new theoretical evidence for a chemically layered mantle, with a perovskitic lower mantle. Our results are obtained from a novel approach for predicting mineral compositions, which is based on the observation that exchange interactions play an important role in determining optimal compositions in Hubbard insulators as well as weak-metals. Our model also provides a solution for the existence of the enigmatic large-low-shear-velocity provinces. We provide evidence for the stability of anomalously Fe-rich brigdmanite, which implies the existence of chemical gradients in the lower mantle. This in turn offers a mechanism for the origin of partial melting and mantle plumes in the lower mantle.

**ACKNOWLEDGEMENTS**

I would like to thank my supervisors Dr Yuanming Pan and Dr John S Tse for supporting me and for helping organize the research and organize my ideas, as well as for providing useful comments, ideas and suggestions. I also thank them for exposing me to other scientific disciplines and research projects, as well as financial contributions. I would also like to thank Dr Wu Min for taking time to teach me some physics and helping me run codes when I was starting the research. I thank Dr Ingrid Pickering for useful suggestions.

**TABLE OF CONTENTS**

## LIST OF TABLES

**LIST OF FIGURES**

**LIST OF ABBREVIATIONS**

| | |
|---|---|
| AE | All electron |
| AFM | Anti-ferromagnetic |
| Bm | Bridgmanite |
| DAC | Diamond Anvil Cell |
| EFG | Electric Field Gradient |
| FM | Ferromagnetic |
| GGA | Generalized-gradient Approximation |
| HSE | Heyd-Scuseria-Erhzerhof |
| IS | Isomer Shift |
| KS | Kohn-Sham |
| LLSVP | Large Low Shear Velocity Province |
| NM | Diamagnetic |
| Ol | Olivine |
| PAW | Projector-augmented Wave |
| PBE | Perdew-Burke-Erhzerhof |
| Pn | Pentlandite |
| Pr | Perovskite |
| PREM | Preliminary Reference Earth Model |
| QS | Quadrupole Splitting |
| SCF | Self Consistent Field |
| SQS | Special Quasirandom Structure |
| XRD | X-ray Diffraction |

# CHAPTER 1

## Introduction

The notion of a chemically layered mantle originated from the observation of chemical differences between mid-ocean ridge basalts (depleted in incompatible elements) and ocean-island basalts (less depleted in incompatible elements) (Hofmann, 1997). Since it is not possible to obtain samples from depths down to the lower mantle, its chemical and mineralogical composition must be inferred by integrating geophysical observations with high-pressure-temperature experiments (Frost, 2008). Knowledge of the composition profile of the mantle, is crucial in determining planetary evolution and dynamics (Kaminsky and Javoy, 2013). Unfortunately, uncertainties in high-pressure-temperature mineral stabilities, as well as physical properties have led workers to ongoing debates about bulk lower mantle compositions, ranging from peridotitic to chondritic (Murakami et al 2012).

A peridotitic lower mantle had long been the most commonly accepted model, whereby the mineralogical constituents are magnesian-silicate perovskite (now formally defined as bridgmanite (Bm) $[\mathrm{Mg, Fe}]\mathrm{SiO_3}$ (Tschauner et al, 2014)), calcium-silicate perovskite and magnesiowüstite/periclase (Pr; $[\mathrm{Mg, Fe}]\mathrm{O}$) (Kesson, 1998). Such a model would imply a lack of chemical layering (atleast in terms of major elements) in the mantle, which is supported by seismic tomographic observations, that sinking, subducted slabs penetrate into the lower mantle (Frost, 2016). However, recent geodynamical modelling indicates that slabs reach the lower mantle, and this is not inconsistent with the chemical layering hypothesis (Ballmer et al, 2015). Furthermore, silicate enrichment in the lower mantle (consistent with the perovskitic lower mantle hypothesis, in which it is assumed that the lower mantle is composed almost exclusively of Fe-bearing Bm) is needed to explain the discrepancy between the upper mantle composition and that of chondritic meteorites (Murakami et al, 2012; Frost, 2016). As

well, the signature of noble gas isotopes supports a primitive reservoir in the lower mantle that is enriched in silica (Moreira et al 2012; Marty, 2012; Mukhopadhyay 2012). This calls for a re-evaluation of the mantle compositional profile model.

Recent experiments suggested that Fe partitions from Bm to other phases at the conditions of the lower mantle (Zhang et al, 2014). However, on a broad scale the perovskitic model remains most plausible, based on comparison with the Preliminary Reference Earth Model (PREM) (Dzewonski and Anderson, 1981), generated from seismic observations (Ricolleau et al 2009; Murakami et al, 2012). Albeit, compositional heterogeneities may be necessary to explain the presence of anomalous large low-shear velocity provinces (LLSVPs) (Mao et al, 2011).

Here, we provide theoretical evidence consistent with a chemically layered mantle, whereby the lower mantle is dominated by Fe-bearing Bm. Our results are based on the observation that mineral compositions can be explained using a simple model of neighbour spin-spin interactions. Geodynamical implications of a perovskitic lower mantle are discussed. We also provide evidence for compositional heterogeneities in the lower mantle, which supports a model capable of reconciling the presence of LLSVPs. Moreover, the presence of chemical heterogeneities provides an additional mechanism for partial melting in the deep Earth and the generation of mantle plumes.

An understanding of the underlying mechanism responsible for driving the variability of mineral compositions is important for not only predicting the composition of planetary materials in exotic conditions (extraterrestrial conditions, planetary interiors, etc.) but also for using mineral properties to make inferences about the environment of formation. The composition of minerals at high pressures and temperatures has generally been determined from high pressure temperature experiments, which however are strongly dependant on complicating factors such as oxygen fugacities, capsule materials, sluggish kinetics of the equilibration and heterogeneity in the samples

(Nakajima et al., 2012).

Here we present the first attempt at understanding the mechanism driving mineral compositions through a first-principles theoretical study. Our analysis shows that exchange interactions may be primordial in governing the compositions of weak metals as well as Hubbard insulator minerals. In doing so, we develop a new method for quickly and easily determining the variability of mineral compositions as a function of pressure and temperature and use this method to predict the composition of the lower mantle. The method is first developed through calculations on the well-known mineral pentlandite (Pn). We then apply and validate the new approach for predicting the compositions of the major phases in the upper and lower mantle as well as the transition zone, whose properties are crucial for describing the mantle convection (Deuss et al, 2006). The success of our approach in predicting these compositions, suggests that the method should prove useful in mapping the mineralogy of planetary interiors. It is noteworthy that the proposed approach does not require total energy calculations to make the compositional predictions. The method is developed from a relation that is observed between the ground-state composition and the magnetic moment of the magnetic species (in this case $Fe$ atoms). We suggest that this relation exists in weak metals and Hubbard insulators (such as the minerals studied here), where the spin degrees of freedom are allowed to fluctuate throughout the solid, even though electrons are relatively itinerant. In fact, volume, density and elemental partitioning changes in these types of minerals have been observed experimentally to coincide with pressure-induced mineral spin-transitions (Lin et al., 2008; Murakami et al., 2005). This supports the hypothesis that exchange interactions are important for driving the variability of mineral compositions.

Most minerals display at least partial disorder (Mustapha et al., 2013). Here, the term disorder denotes the fact that the position of an atom does not depend on (or is not correlated with) the

position of other atoms in the crystal lattice. Accurate modeling of compositional variations in minerals and other crystalline solids has previously been hampered by this treatment of disorder. The simplest case is that of perfect disorder, where atomic positions are completely uncorrelated. This corresponds to the high-temperature limit, where configurational entropy is a maximum. Although approximate, the case of perfect disorder has been proven to be successful in describing the properties of metamorphic and igneous phases (Sarmiento-Perez et al., 2014; Efthimiopoulos et al., 2015; Skelton et al., 2015). Here, we adopt the perfect disorder approximation by using the Special-Quasi-random Structure (SQS) approach (Kikuchi et al. 1951; Sanchez et al. 1984; Van de Walle et al. 2013). This SQS approach allows us to determine the optimal distribution of the atoms by matching a specified set of correlations (or cluster functions) between the neighboring atoms to the corresponding correlations of the perfectly disordered state. In this way, the SQS approach provides the best periodic supercell approximation to the true disordered state (Van de Valle et al., 2013).

## CHAPTER 2

## Methods

In the SQS approach, $\boldsymbol{\sigma}$ denotes the vector of lattice site compositions, $\sigma_i$ for lattice site $i$. We have $\sigma_i \in [0, M_i - 1]$ if there are $M_i$ distinct chemical components at the site $i$ (Van de Walle et al, 2013). We call correlation the quantity which determines how the composition of one lattice site depends on the composition of all other lattice sites. Our task consists of finding the set of compositions $\boldsymbol{\sigma}$ which yield the lowest correlation for all lattice sites. The set of sites of a particular correlation is called a cluster, denoted by $\boldsymbol{\alpha}$, whose length spans all lattice sites. We set $\alpha_i = 1$ if site $i$ belongs to $\boldsymbol{\alpha}$, and $\alpha_i = 0$ if site $i$ does not belong to $\boldsymbol{\alpha}$. In accordance with the Ising lattice model, we define the correlation $\rho_\alpha(\boldsymbol{\sigma})$ associated with cluster $\boldsymbol{\alpha}$ as a symmetrized average over cluster functions $\Gamma_{\boldsymbol{\alpha}}(\boldsymbol{\sigma}) = \prod_i \gamma_{\alpha_i, M_i}$(Sanchez et al., 1984; Van de Walle et al., 2013):

$$\rho_\alpha(\boldsymbol{\sigma}) = \left\lfloor \prod_i \gamma_{\alpha_i', M_i}(\sigma_i) \right\rfloor_{\boldsymbol{\alpha}}, \qquad (1)$$

where the product runs over all lattice sites and $\lfloor \dots \rfloor_{\boldsymbol{\alpha}}$ is the average taken over all clusters $\boldsymbol{\alpha}'$ equivalent by symmetry to $\boldsymbol{\alpha}$. To find the optimal configuration of atoms, the correlation of a candidate structure $\rho_\alpha(\boldsymbol{\sigma})$ must match that of the perfectly disordered state $\rho_\alpha(\boldsymbol{\sigma^{rnd}})$. For a perfectly disordered state, site occupations are completely independent. Hence, the symmetrized average over cluster functions in equation (1) becomes a simple product over the average composition of all lattice sites:

$$\rho_\alpha(\boldsymbol{\sigma^{rnd}}) = \left| \prod_i \gamma_{\alpha_i', M_i}(\sigma_i^{rnd}) \right|_{\boldsymbol{\alpha}} = \prod_i \left| \gamma_{\alpha_i', M_i}(\sigma_i^{rnd}) \right|_{\boldsymbol{\alpha}} . \quad (2)$$

The correlation difference for a candidate SQS can then be strictly defined as $\Delta\rho_\alpha(\boldsymbol{\sigma}) = \rho_\alpha(\boldsymbol{\sigma}) - \rho_\alpha(\boldsymbol{\sigma^{rnd}})$. Finding the optimal SQS then consists of minimizing an objective functional of the following kind:

$$Q = -\omega L + \sum_{\boldsymbol{\alpha} \in \boldsymbol{\mathcal{A}}} |\, \Delta\rho_\alpha(\boldsymbol{\sigma})| \,, \quad (3)$$

where $L$ is the largest $l$ such that $\Delta\rho_\alpha(\boldsymbol{\sigma}) = 0$ for all clusters with $diam(\boldsymbol{\alpha}) \leq l$. $\boldsymbol{\mathcal{A}}$ is a user specified set of clusters and $\omega$ is a user specified weight. The first term of $Q$ represents the fact that the quality of a candidate SQS should reflect the number of clusters that are matched exactly and the second term assures that the optimal SQS approaches perfect disorder (Van de Walle et al, 2013). Here, $Q$ is minimized by sampling configurations using a simulated annealing procedure. This procedure has been implemented in the *mcsqs* code of the *Alloy Theoretic Automated Toolkit* (Van de Walle et al, 2013).

Once the optimal configuration of atoms is obtained, the ionic, magnetic and electronic degrees of freedom are relaxed by solving the SCF-Kohn-Sham equations. In doing so we use the spin-polarized GGA Hamiltonian of Perdew, Becke and Ernzerhof (1996) (PBE), as is usually done for metallic systems and materials with small band gaps. However, it is well known that the PBE Hamiltonian fails to properly describe the exchange and correlation effects in 3d and higher energy level electrons. To circumvent this problem, we adopt an effective Hamiltonian as proposed by

Hubbard (1968). The orbital-dependent potentials of Hubbard (1968) are implemented using the rotationally-invariant form proposed by Duradev et al. (1998), which includes corrections to the total energy according to the first-order term in the multipolar Coulomb and Exchange series (Term containing radial Slater integrals of the form $F^0$). A Slater integral denotes a Coulomb or Exchange Hartree-Fock integral of the form $\langle \psi_a \psi_b | \hat{O} | \psi_c \psi_d \rangle$, where the $\psi_i$ are normalized Slater functions (i.e. analytical solutions of the one-electron Schrödinger equation) and the indices $a, b, c, d$ generally combine a set of sequential numbers and cell indices. $\hat{O}$ is an operator consisting of a sum of terms, where each term is inversely proportional to the distance between the centers of the Slater functions. Here $F^k$ denotes the radial part of these integrals in the $kth$ order of the multipolar expansion of $\hat{O}$. In this manner orbital energies, described as the self-consistent expectation values of the Kohn-Sham Hamiltonian are calculated as follows:

$$E_m = E_{PBE} + \frac{U_{eff}}{2} \sum_{\mathcal{s}} \left( n_{m,\mathcal{s}} - n_{m,\mathcal{s}}^2 \right) , \tag{4}$$

where $m$ denotes the momentum quantum number, $\mathcal{s}$ is the spin quantum number, $U_{eff}$ is the effective Coulomb parameter and $n_{m,\mathcal{s}}$ is the (second-quantized) spin density. Equation (4) displays the well-known behavior of $U_{eff}$, which introduces an energy penalty to the pertinent functional which favors integer occupation (full or empty) of the orbital manifold over partial occupations. Specifically, we use $U_{eff} = 4.5eV$ for 3d electrons in Fe and $U_{eff} = 6.0\ eV$ for 3d electrons in Ni (Aryasetiawan et al, 2006; Duradev et al, 1998). Justification for the choice of these values is provided in the following sections.

Broullion zone sampling are performed on a 4*4*4 Γ-centered mesh, where Γ denotes the center point of the first Broullion zone. Gaussian finite-temperature smearing of the one-electron energy levels was used. The crystalline-orbitals were expanded with a plane-wave basis set with a 400 eV energy cut-off. Electron-ion interaction were treated within the Projector-Augmented-Wave (PAW) potentials (Blochl, 1994). Here, the d, semi-core s and p states are treated as valence electrons. Semi-core states consist of plane waves which intersect the augmentation and valence regions of the PAW potentials. The Kohn-Sham Hamiltonian was diagonalized with a band-by-band generalized minimal residual minimization method. The ionic degrees of freedom were optimized through conjugate-gradient minimization of the total energy, using the Hellmann-Feynman forces (Kresse et al, 1996). The relaxation of the electronic and ionic degrees of freedom were considered to have converged when the change in the total (free)-energy (and eigenvalues of the KS Hamiltonian for the electronic loop) between two subsequent relaxation steps did not exceed 400 eV. These tolerances were found to give converged results for lattice geometries and energies of formation. Tighter tolerances are used for calculation of other observables (see below). Since the systems are magnetic, calculations with the spin unrestricted formalism were performed. This relaxation of the ionic, magnetic and electronic degrees of freedom was performed using the *VASP* code (Kresse et al, 1996).

The Mossbauer QS and IS values reported in the thesis were calculated using the following formulas:

$$\mathrm{QS} = \frac{1}{2} eMV_{zz} \left(1 + \frac{\eta^2}{3}\right)^{\frac{1}{3}} \tag{5}$$

$$IS = \alpha[|\psi(0)|^2 - |\psi_{bcc}(0)|^2], \tag{6}$$

where $e$ is the elementary charge, $M$ is the quadrupole moment of the relevant nucleus (in our case $Fe^{57}$), $\eta$ is the asymmetry parameter $\left(\eta = \left|V_{yy} - V_{xx}\right|/|V_{zz}|\right)$, if $|V_{zz}| \geq \left|V_{yy}\right| \geq |V_{xx}|$ are the eigenvalues of the $3 \times 3$ EFG tensor. $|\psi(0)|^2$ is the electron density extrapolated to the nuclear position for the system under consideration, while $|\psi_{bcc}(0)|^2$ is the corresponding value for body-centered-cubic $\alpha - Fe$. Finally, $\alpha$ is an element-specific nuclear calibration constant. Here, we use the ubiquitous values of $\alpha = -0.24\ a_o^3\ mm\ s^{-1}$ (Blaha and Schwarz, 1988) and $Q = 0.16\ barn$ (Dufek et al., 1995) for $Fe^{57}$.

The calculation of the elements of the magnetic susceptibility tensor $\chi_{ij}$ is achieved using a reciprocal-space finite-difference formula of the form (Yates et al, 2007):

$$\chi_{ij} = \lim_{q \to 0} \frac{F_{ij}(q) - 2F_{ij}(0) - F_{ij}(-q)}{q^2}, \tag{7}$$

where $F_{ij}$ are quantities which include effects of perturbation of the PAW pseudo-wavefunction in first order with respect to the applied field and contains corrections for the difference in the norm of the PAW pseudo-wavefunction and the true wavefunction inside the augmentation region (Yates et al, 2007). Here, we use the value $q = 0.001$. These derivatives are evaluated by interpolating the PAW projectors to $q$ in reciprocal space using a cubic spline. The magnetic susceptibility (and magnetic moment calculations of Figures 3 and 6) were performed using tighter tolerances of 500 eV for the plane-wave energy cutoff and energy convergence criterion for the electronic SCF loop. These are the highest tolerances that were computationally feasible using our available resources.

# CHAPTER 3

# Results

## 3.1 Pentlandite

The mineral pentlandite [Pn, $(Fe, Ni)_9S_8$] is known to have a composition that clusters around $\frac{Fe}{(Fe+Ni)} \approx 0.4 - 0.6$ in terrestrial rocks, despite the fact that this mineral has been documented to occur in diverse geological environments and lithological associations (Laznicka, 2013). Also intriguing is the fact that even though Pn occurs mostly as a ternary Fe-Ni-rich phase with $\frac{Fe}{(Fe+Ni)} \approx 0.5$, Pn with $\frac{Fe}{(Fe+Ni)} \approx 0.7$ has been reported to occur in meteorites by Hoffman et al. (2001) and Ni-free Pn has been synthesized by Nakazawa et al., (1973).

Figure 1(a, b) shows the unit cell and dominant features of the crystal structure of Pn. Metal clusters consisting of eight tetrahedrally coordinated metal atoms occur across unit cell boundaries. The tetrahedral metals are bonded to three face-capping sulphurs and one bridging sulphur. The bridging sulphur atoms connect tetrahedrally-coordinated metal clusters through bonding with the octahedral metals.

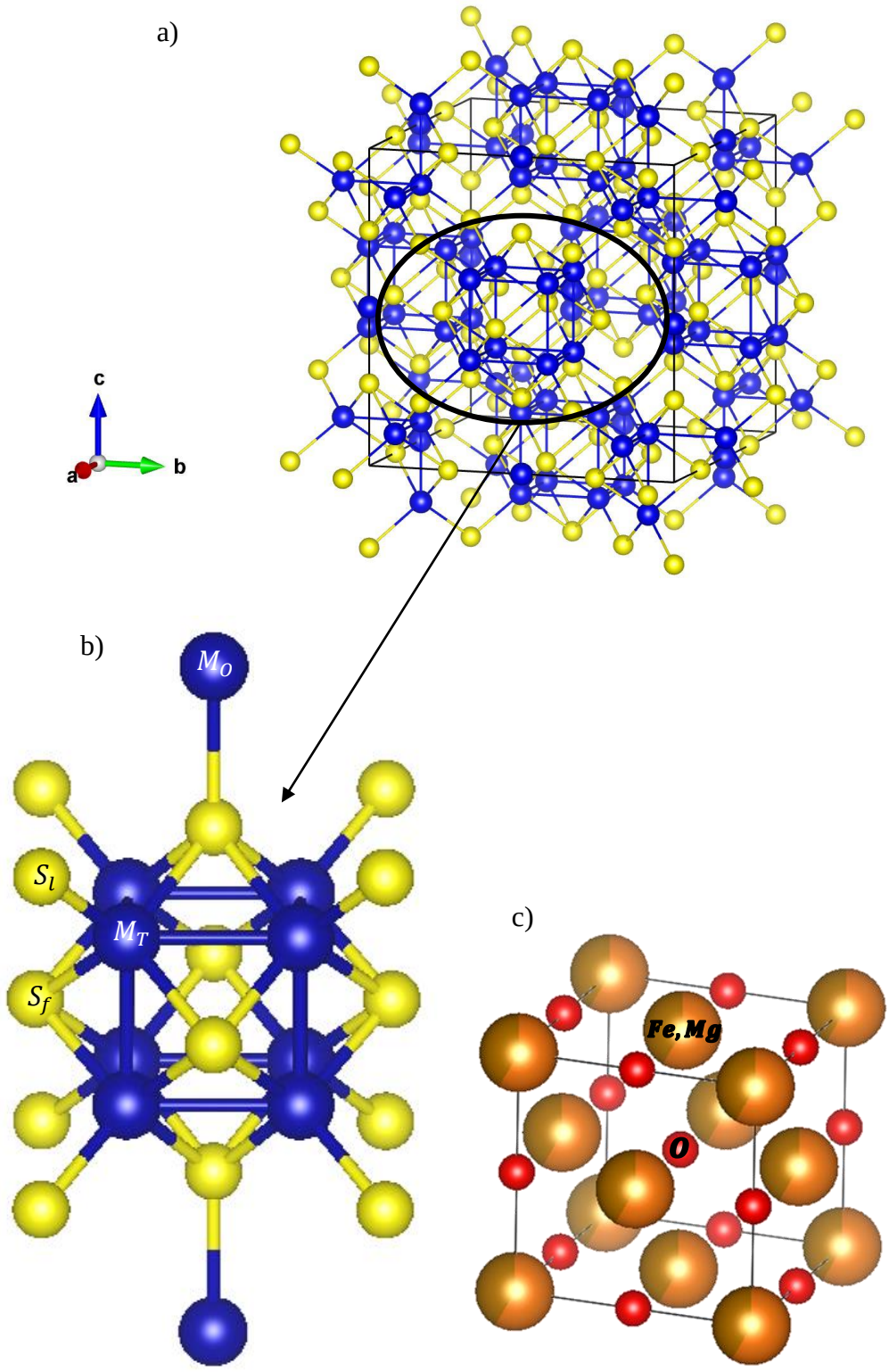


**Figure 1:** (a) Pn unit cell and (b) metal sulphide cluster occurring in Pn unit cell. The cluster consists of eight tetrahedral metal $(M_T)$ atoms. The $M_T$ are bonded to three face-capping $(S_f)$ sulphurs and one bridging sulphur $(S_l)$. The $S_l$ link the clusters through bonding with octahedral metals $(M_O)$. (c)

Periclase unit cell.

In the minimization of the $Q$ functional (see equation 3), two-body correlations are matched up to the sixth nearest neighbor, three-body and four-body correlations are matched up to the 2nd nearest neighbours. We used a 2*2*1 supercell consisting of 68 atoms, which is sufficiently large to guarantee the stability of the SQS solution. We used the weight $\omega$ =1 (see equation (3)) and the $Q$ functional is minimized for simulated annealing temperatures of 1, 10 and 100 [unit-less]. The minimization was considered to have converged when sixteen independent samplings of $Q$ yield the same result. The correlation differences $\Delta\rho_{\alpha}(\boldsymbol{\sigma})$ reach the same values regardless of the simulated annealing temperature. This suggests that a global minimum in $Q$ has been reached and the optimal structure has been obtained (at least for the chosen set of clusters and supercell size). The obtained correlation differences can be found in the supplementary material.

The extracted lattice and atomic parameters from the SQS approach are then used as a starting point to solve the KS-SCF equations. It is noteworthy that calculations performed with $U_{eff} = 0$, or with halved the $U_{eff}$ values for 3d states predicted diamagnetic structures, in disagreement with the observed paramagnetic behaviour (Knop et al., 1975); the extracted energy of formation patterns did not vary as a function of composition, which is also incorrect. To validate the chosen $U_{eff}$ (*vide supra*) value, we have computed the Mossbauer Quadrupole splitting (QS) data for the terrestrial Pn compositions ((Fe/((Fe+Ni) )=0.56). The theoretical values of 0.33 mm/s to 0.56 mm/s are in reasonable agreement with the experimental values of ~0.3 mm/s (Knop et al., 1975). To further test the choice of $U_{eff}$ we calculated the total-energy and Mossbauer parameters of Pn using the Range-separated hybrid HSE06 Hamiltonian and an all-electron (AE) localized basis-set using the program

CRYSTAL14 (Dovesi et al, 2014). We adopted the geometric and magnetic information retrieved from the PAW/PBE+U results as the initial inputs. Further details on the AE calculation can be found in the supplementary information. The AE calculation yielded a QS of ~0.55-0.7 mm/s, in agreement with the PAW/PBE+U result. We also extracted the isomer shift (IS) of Pn from the electron density difference (between body-centered-cubic Fe and Pn) at the nuclear position. This yielded IS values of ~0.234 mm/s and ~0.293 mm/s for the octahedral and tetrahedral Fe sites, respectively, again in reasonable agreement with the experimental results of 0.22-0.36 mm/s and 0.46-0.65 mm/s (Knop et al., 1975). For the extraterrestrial Pn composition $\left(\frac{Fe}{(Fe+Ni)} = 0.7\overline{2}\right)$, the AE calculations yielded IS values of ~0.175-0.199 mm/s, as compared to the experimental result of ~0.4 mm/s reported by Hoffman et al (2001). The minor discrepancies between the calculated and measured Mossbauer parameters are most likely the result of the inability of the hybrid and GGA+U Hamiltonians to describe the sphericity of core charge distributions, as was noted by other authors (Casassa and Ferrari, 2016; Sinnecker et al, 2005; Nemykin and Hadt, 2006).

For comparing the obtained magnetic structures with experimental data, we have calculated the $3 \times 3$ magnetic susceptibility tensor $\hat{\chi}$ of terrestrial Pn using the linear response formula of Yates et al. (2007). $\hat{\chi}$ is diagonalized to $\overline{\chi}$ and we report the value $\chi = Tr[\overline{\chi}]/3$, which is a scalar that can be compared to the experimental results. Here, $Tr$ denotes the trace operator. We obtain a value of $\chi = 1.4$E-5 emu/g, in comparison with the 0.977E-5 emu/g (extrapolated to 0 °K) of Knop et al. (1975). Unfortunately, we cannot directly compare the calculated total unit cell dipole moment to any experimental value, because the magnetic susceptibility of Fe-Ni Pn has not been measured in the regime over which the Curie law holds, so that no simple relation exists between measured susceptibility and mean magnetic moment.

Figure 2 shows the energies of formation that were determined by independently computing

the total energies of Pn for various compositions, as well as crystalline Ni, Fe and S in their ground states using the PAW/PBE+U Hamiltonian. The black circles represent solutions obtained when an initial antiferromagnetic (AFM) spin-configuration was assumed, the blue stars denote those obtained from an initial ferromagnetic (FM) state and the red crosses are for an initial non-magnetic (NM) state. These calculations are performed from SQS solutions whereby the Fe concentration in the 32 tetrahedral sites are scaled proportionately to the composition, whereas the 4 octahedral sites contain only Fe for Fe-rich compositions (50% Fe and over), and only Ni for Ni-rich compositions (less than 50% Fe). The red diamonds in Figure 2 represent the solution obtained using an initial FM state and a second site-occupation mixing model (model 2), whereby both octahedral and tetrahedral site compositions are scaled proportionately to the global composition (i.e., site-occupancies of Ni and Fe are less than unity in both octahedral and tetrahedral sites). Of course, in all cases the magnetic degrees of freedom were subsequently relaxed. We find a minimum in the energy of formation when the supercell contains about 26 Fe atoms $\left(\frac{Fe}{(Fe+Ni)} = 0.7\bar{2}\right)$, which represents the extraterrestrial Pn composition. The fact that our ground state calculations find a minimum in the energy of formation near the extraterrestrial Pn composition but not the terrestrial Pn composition should not come as a surprise. Experimental phase diagrams have previously suggested that Pn occurs as a more Fe-rich phase at lower temperatures (Harris and Nickel, 1972). At higher temperatures, a minimum in the energy of formation might be found to occur at the terrestrial composition $\left(\frac{Fe}{(Fe+Ni)} \approx 0.5\right)$. A local minimum in the energy of formation for the second mixing model (red diamonds in Figure 2) is not clearly seen near the terrestrial composition. However, this minimum will become clearer in Figure 4 (see text below for explanation), suggesting a stable phase under different thermodynamic conditions.

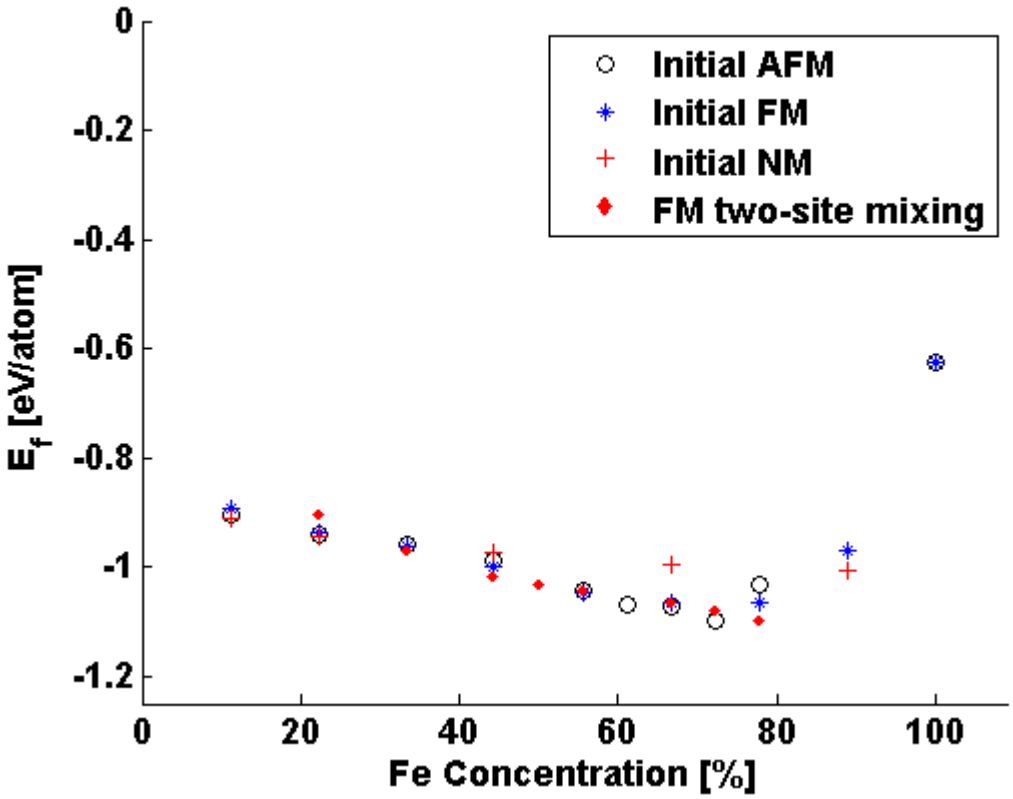


**Figure 2:** Energies of formation of Pn as a function of composition. The black circles are for initial antiferromagnetic states, the blue stars are for initial ferromagnetic states, the red crosses are for initial non-magnetic states and the red diamonds are for initial ferromagnetic states, using the second site-mixing model.

An understanding as to why an energy minimum occurs at the extraterrestrial composition can be gathered from Figure 3. These figures are plots of the energy of formation and the total magnetic moment per supercell as a function of the Pn composition. These plots are generated from the set of Pn structures, which give a minimum for their respective compositions. Figure 3 shows that a local (and not global) minimum exists in the magnetic moment per supercell at the extraterrestrial composition. This is because the Fe atoms systematically have higher individual magnetic moments

than Ni atoms. Therefore, as the composition varies from Fe-rich to Fe-poor, the magnetic moment per supercell decreases as a result of changes in the bulk composition. The effects of bulk composition can be removed by normalizing the magnetic moment per supercell by the number of Fe atoms in the cell. This results in a normalized magnetic moment, which does have a global minimum at the extraterrestrial Pn composition.

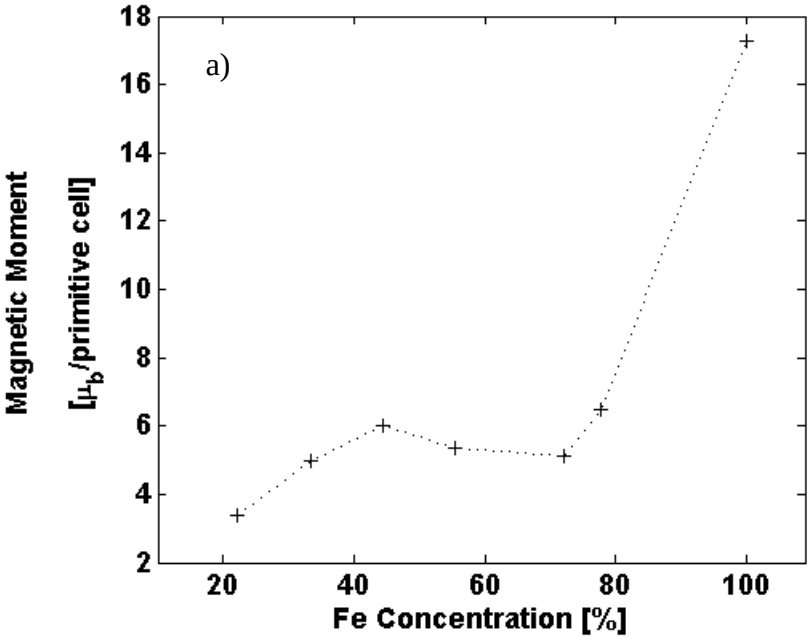


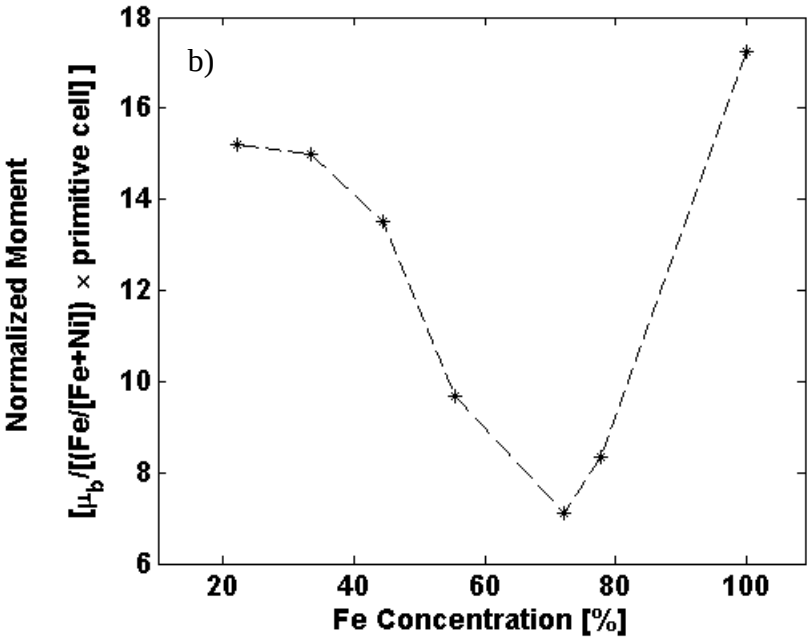

**Figure 3:** Plot of the (a) total primitive cell magnetic moment, (b) normalized magnetic moment as a function of Pn composition.

The existence of this relation between the magnetic moment and the formation energy suggests that exchange interactions are important in dictating the Pn composition. Our calculations retrieve atomic magnetic moments of $\sim 3\ \mu_b$ for the Fe atoms, $\sim 1\ \mu_b$ for the Ni atoms and negligible moments for S atoms. Assuming that the magnetic Fe-atom centers account for most exchange interacts in the crystal, we can simplify the exchange interactions as neighbour Fe-Fe spin-spin interactions within n-body clusters of finite radius. The Fe-Fe spin-spin interactions can be of direct exchange type (in which the Fe atoms are nearest neighbours), or of superexchange type (in which the Fe atoms interact through a non-magnetic S anion). Under these assumptions, the relation between the magnetic moment and the formation energy translates to a relation between the number of the Fe-Fe neighbours in the n-body clusters and the formation energy.

We plot the number of the Fe-Fe neighbours of the clusters as a function of composition for both site-mixing models in Figure 4. These curves were generated starting from the ambient-pressure neutron powder diffraction crystal structures of Tenailleau et al. (2006) and using our site occupancies obtained from the SQS calculations. We find that the curves reach a stable solution using a diameter of 10 $\dot{A}$ for the clusters. This diameter is also used for all subsequent figures of this type, unless otherwise specified. The curves show that the number of Fe-Fe neighbours generally increase as the composition becomes more Fe rich. Sharp drops in the curves occur at more stable compositions, because a smaller number of Fe-Fe neighbours corresponds to a decrease in exchange interactions, which in turn lowers the magnetic moment and the formation energy. The black curve (representing the first (one-site) mixing model at 298 K) shows a sharp decrease at the extraterrestrial composition,

in agreement with the total-energy calculations. The red curve (second (two-site) mixing model at 298 K) has sharp drops both at the terrestrial and extraterrestrial compositions, again in agreement with the local and global minimums found at these compositions for the same mixing model with the total-energy calculations. The blue curve (two-site mixing, 573 K) shows a drop at the terrestrial composition and a less pronounced drop at the extraterrestrial composition. These results further support the hypothesis that the terrestrial composition is favoured at high temperatures. Again all these compositional predictions made with Figure 4 did not require total-energy calculations. A code for calculating and plotting curves similar to those in Figure 4 is provided in Appendix II.

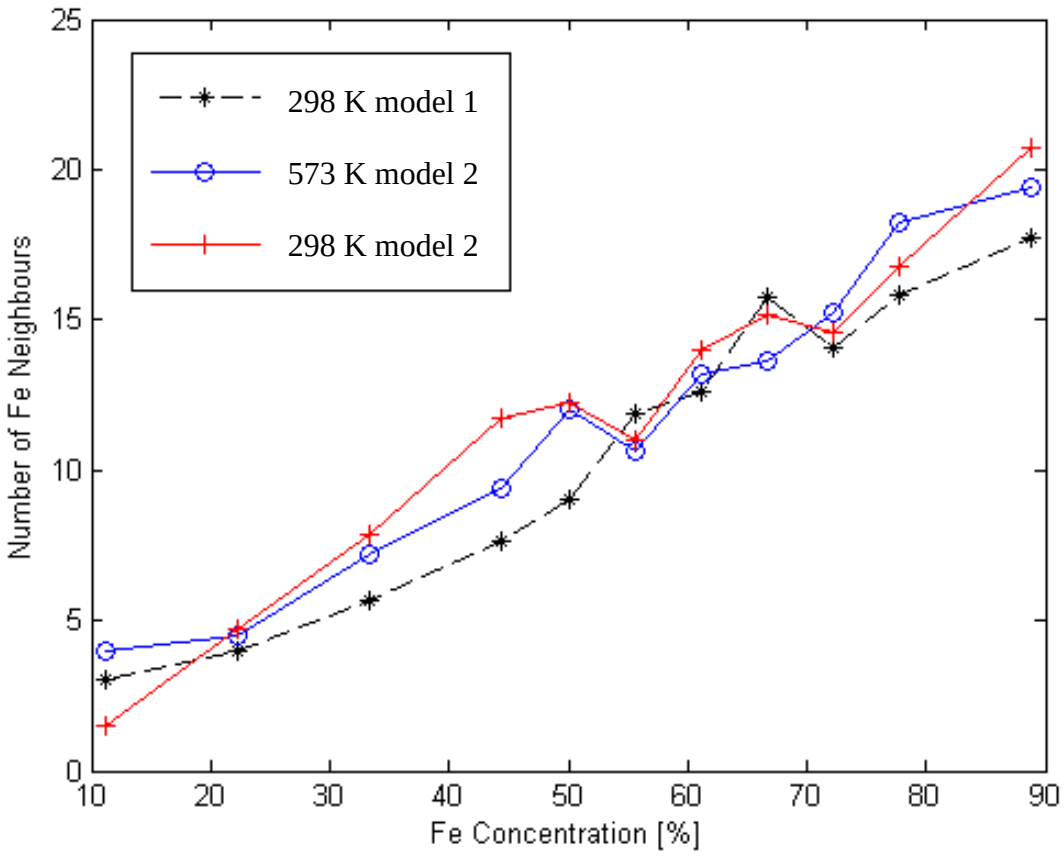


**Figure 4:** Number of Fe-Fe neighbors inside the n-body clusters as a function of Pn composition. The black curve is for the first (one site) mixing model at 25 °C, while the blue and red curves are for the second (two-site) mixing model at 300 and 25 °C, respectively.

### 3.2 Application to Principle Phases in the Upper Mantle and Transition Zone

To further demonstrate that how plots similar to Figure 4 can be useful in determining compositional changes as a function of thermodynamic variables, we validate the method through applications to the dominant phases involved in the transitions at the 660 km mantle discontinuity, as well as the upper mantle. These phases are olivine (Ol; $[\mathrm{Mg, Fe}]_2\mathrm{SiO}_4$) (the principal phase in the lithospheric mantle); as well as ringwoodite (Rw; $[\mathrm{Mg, Fe}]_2\mathrm{SiO}_4$), Bm and Pr. The discontinuity from the upper mantle to the transition zone is vital in determining the mantle convective style (Hofmann, 1997; Schubert, et al., 2001). It is marked by seismic reflections over a wide range of depths, which may require the existence of multiple phase transitions (Deuss et al, 2006). It has been inferred that at ~24 GPa (660 km depth), Rw transforms to an assemblage of Bm and Pr (Frost, 2008). The crystal structure of Pr is shown in Figure (1c), which is a simple face-centered cubic unit-cell. We performed the SQS calculations on these systems using an approach similar to that developed for Pn. More details can be found in the supplementary information.

For Pr, we use the 0 GPa and 25 GPa X-ray diffraction crystal structures of Fei et al. (1992) as the starting models. Figure 5(a) shows the obtained neighbour analysis curves for Pr at 0 GPa, 573 K (in red) and at 25 GPa, 803 K (in black). The low pressure curve has a dip at an Fe concentration of ~0.5. The high pressure curve has a dip at an Fe concentration of ~0.35. These Pr compositions are in agreement with the experimental results of Frost and Langenhorst (2002), Ozawa et al. (2008) and Nakajiwa et al., (2012). The Rw curve in Figure 5(b), which was generated from the X-ray diffraction crystal structure of Hazen et al (1993) (1673 K, 22 GPa), shows a dip at a Fe concentration of 0.15, which is in agreement with the experimental result of Frost et al (2001). For Ol, we use the ambient condition crystal structure of Merli et al (2001). The results presented in Figure 5(c) display a dip at an Fe concentration of ~0.2, which is within the range of the Ol compositions observed in mantle

xenoliths (Bernstein et al, 2007).

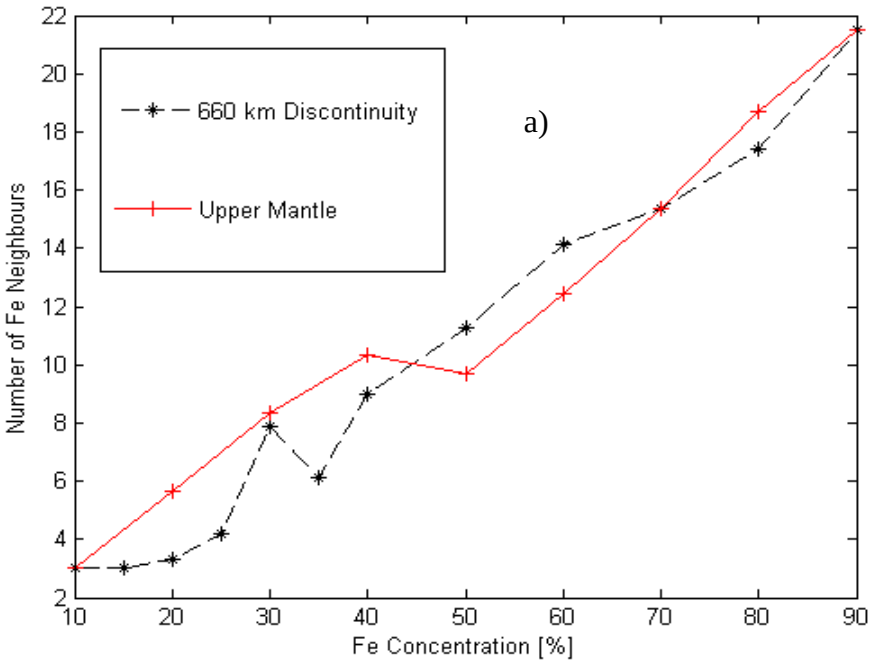


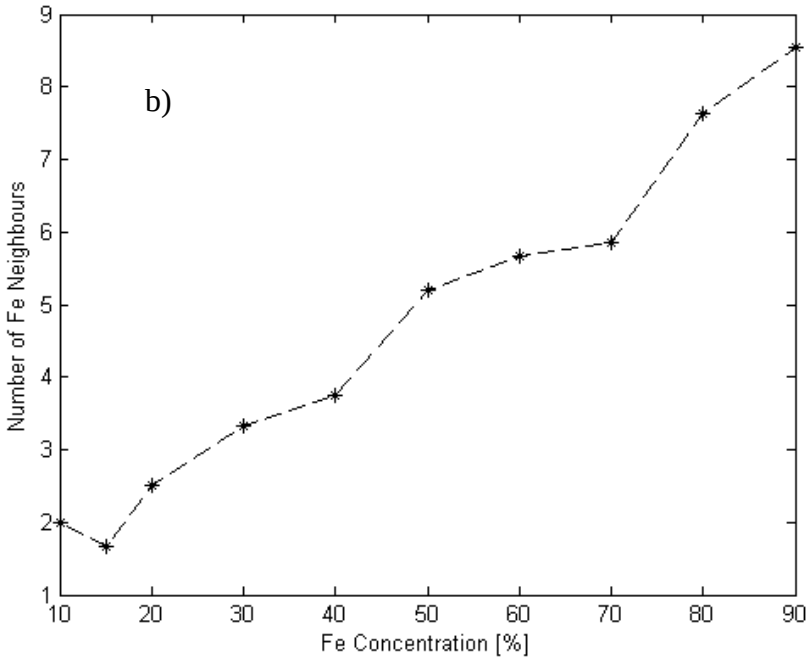

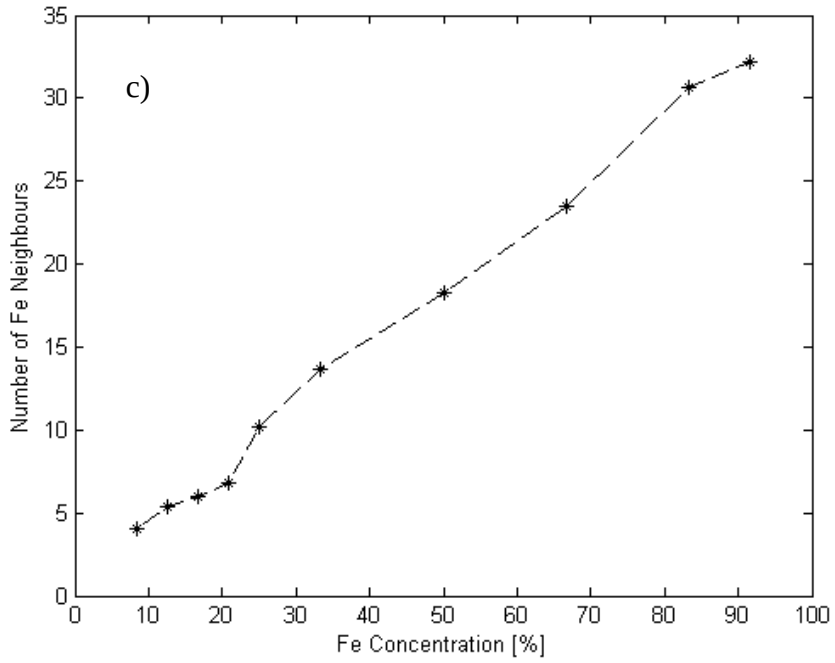


**Figure 5**: Fe Neighbour analysis plots for (a) Pr, (b) Rw (c) Ol (d) Bm.

In order to validate the importance of exchange interactions in predicting these mineral compositions, we have performed total-energy calculations at 25 GPa, on the Pr series. Using a $U_{eff} = 4.5eV$ for Fe 3d states, and an Fe concentration of 0.35, we obtain a QS value of ~1.34 mm/s at 25 GPa, compared to the experimental result of Lin et al. (2009) of ~1.05 mm/s of Pr with a Fe concentration of 0.25 at 20 GPa. We obtain a slightly closer agreement with the experiment using a $U_{eff} = 3.5\ eV$ for Fe 3d states of ~1.27 mm/s. More importantly, using $U_{eff} = 3.5\ eV$ allow us to ensure that the solution converges to a Fe-high-spin-state solution for most Fe atoms, to maintain agreement with previous theoretical and experimental studies (see Tsuchiya et al, 2006 and references therein). As a result, we use the $U_{eff} = 3.5\ eV$ for calculations on the rest of the series. This value of $U_{eff}$ deviates slightly from the values proposed by Tsuchiya et al (2006), which we

attribute to the fact that their calculations are based on the local density approximation, whereas ours are based on GGA, as well as different approximations involved in the treatment of the on-site Coulomb interactions. For the purposes of this study, we limit the calculations only to the high pressure case. At lower pressures, different effective Coulomb parameters would be required, because the effects of localized d-electron correlations are expected to decrease with pressure. Furthermore, resolving the magnetic structures of the Pr series at low pressures most likely requires a more explicit treatment of higher order terms in the multipolar Coulomb and Exchange series (correction according to approximate treatment of radial Slater integrals of the form $F^2, F^4, F^6$, see methods section) for the description of the on-site Hubbard term, and these are not captured by equation (4) (which only considers corrections due to approximate treatment of $F^0$). Figure (6) shows the variation of the total energy and normalized magnetic moment for the Pr series at 25 GPa, which have minimums at the Fe concentration of ~0.35, as predicted by the neighbour analysis curves.

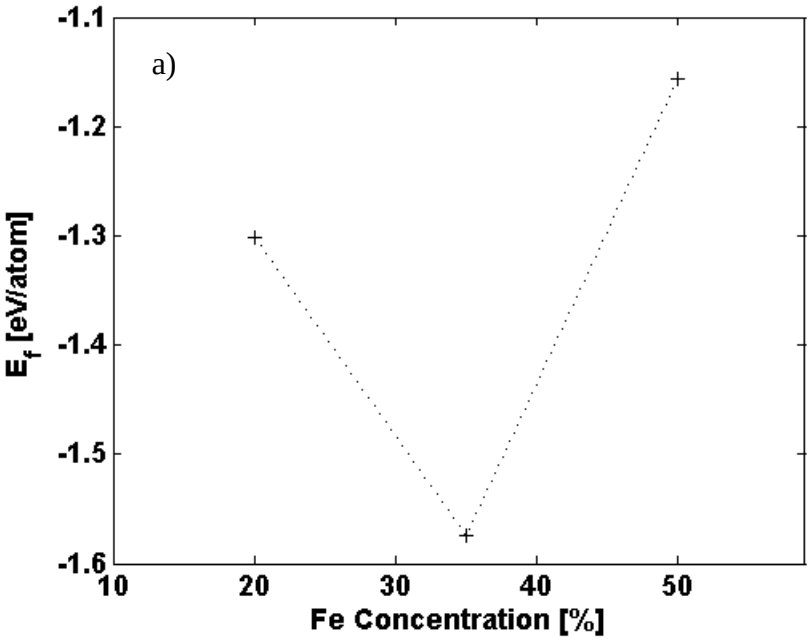

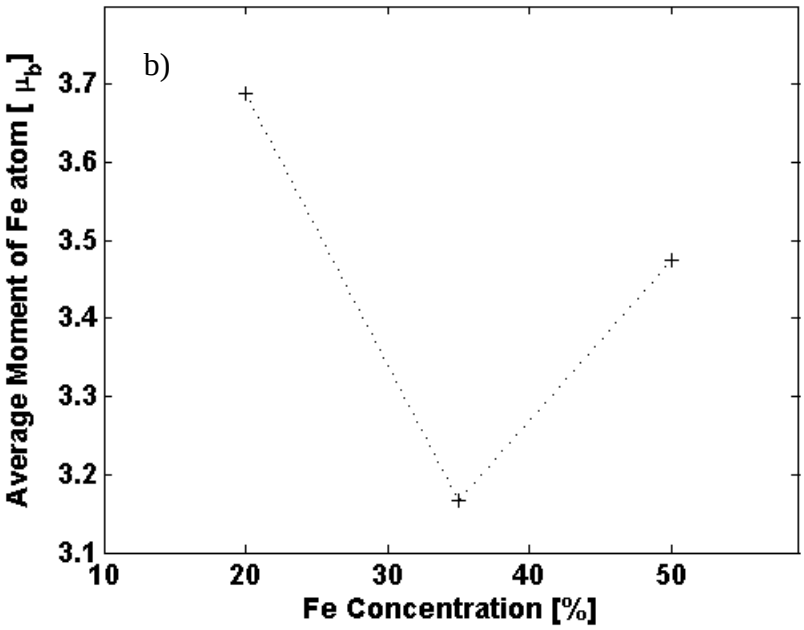


**Figure 6:** (a) Energy of formation of Pr as a function of composition (b) average magnetic moment of the Fe atoms as a function of composition, which we report instead of the quantity in Figure 3(b), as here Fe are the only magnetically active atoms.

### 3.3 Predictions on the Lower Mantle Compositions

The neighbour analysis method is now applied to predict the composition of Bm at conditions relevant to the 660 km mantle discontinuity, as well as the lower mantle. The curve relevant to the 660 km mantle discontinuity was generated from the XRD crystal structure of Jephcoat et al (1999) (1920 K, 25 GPa). The lower mantle curve was generated using the unit-cell parameters of Zhang et al. (2014) (2300 K, 101 GPa), who determined the variation of the Bm parameters in a laser-heated diamond anvil cell (DAC). Solid-state reactions in the DAC, as well as other experimental difficulties preclude refinement of the crystal structure of the Fe-bearing Bm phase at the lower mantle conditions. As a result, the lower mantle Bm Wyckoff positions were extracted from the Mg end-member phase of Fiquet et al (2000) (2500 K, 94 GPa). Zhang et al (2014) predicted a nearly Fe-free Bm composition at these conditions, so the Wyckoff position of Fiquet et al. (2000) should be compatible with their lattice parameters. Regardless of possible uncertainties in the Bm crystal structure we predict a more Fe-rich composition using the end member parameters, so Wyckoff positions from an Fe-bearing Bm experiment would not change our results and conclusions.

Figure 7 shows that the obtained neighbour analysis curve relevant to conditions at the 660 km mantle discontinuity has a dip at an Fe concentration of ~0.12, which is in agreement with the experimental composition of Frost and Lagenhorst (2002). The curve relevant to conditions of the lower mantle also has a dip at an Fe concentration of ~0.12, which is a composition that is consistent with models that predict a compositionally layered mantle with a perovskitic (more silicic) lower mantle. Interestingly, a dip in the curve also occurs at an Fe concentration of ~0.23, suggesting that both of these compositions are stable at lower mantle conditions. This finding is consistent with the experimental result of Mao et al (2011), who found that the anomalously low shear-wave velocities of LLSVPs can be reconciled by the presence of Fe-rich Bm in the lower mantle. Their experiments were

performed on Bm with an Fe concentration of 0.25, which is very close to our predicted Fe-rich composition.

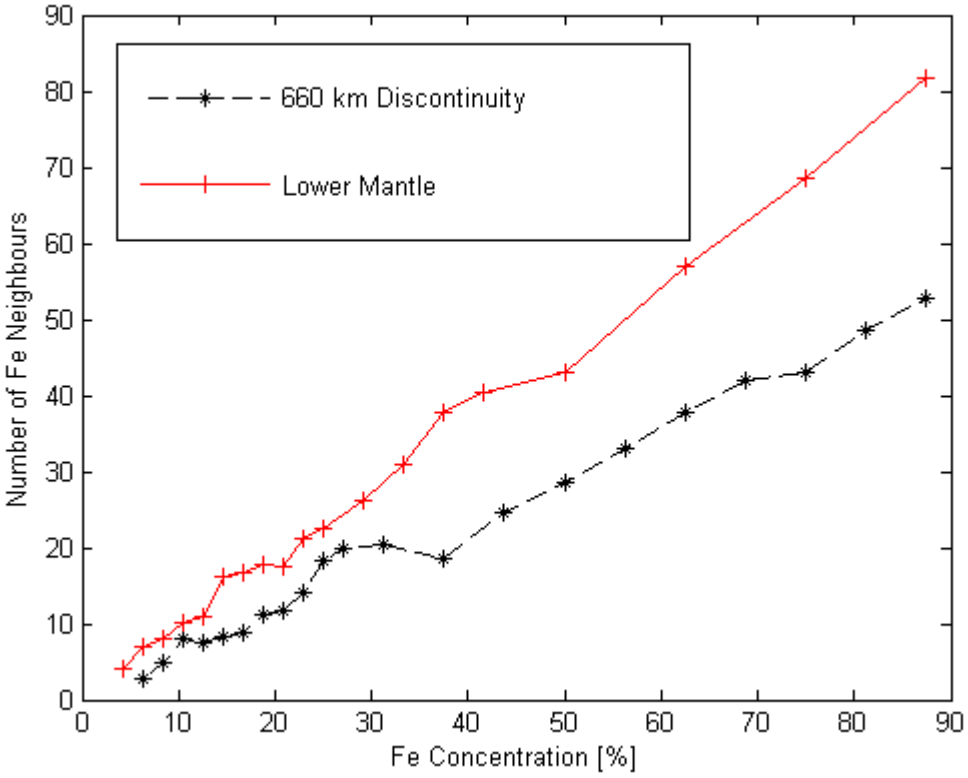


**Figure 7.** Neighbour analysis curves for Bm crystal structures relevant to conditions at the 660 km mantle discontinuity and the lower mantle.

## CHAPTER 4

## Discussion and Conclusion

In the calculation of the curves of Figures 4, 5, 7, convergence of the shape of the curve and position of the minima was thoroughly checked with regards to all computational parameters. These parameters are the size of the supercell, the number of matched cluster functions, the value of the fictitious simulated annealing temperature and the radius of the spheres involved in enumerating the number of Fe-Fe neighbours. The only sources of errors in the curves present in Figures 4, 5 and 7 can therefore be considered to be errors in the SQS approximation (perfect disorder or high-temperature limit), as well as negligible numerical errors. However, as stated and referenced in the introduction, the SQS approximation has been successfully applied to igneous and metamorphic phases, which are also even lower temperature phases than the mantle phases studied here. We therefore expect that the SQS approximation should be sufficient for our purposes.

The curves of Figure (7) and Figure (5b) have minima and compositions which are inconsistent with the experimental compositions (Fe concentration of 0.35 and 0.5 for Figure (7) and Fe concentration of 0.4 and 0.7 for Figure (5b)). This occurs because our calculations generate a set of favourable structures (in the sense of minimizing exchange interactions) which cannot always unambiguously predict the lowest-energy composition at a particular thermodynamic conditions. The set of minima not corresponding to the experimental composition may either not occur in nature because it is not permitted by the bulk composition of the system (for example: not enough Fe available at onset of crystallization), or because these compositions are de-stabilized by other factors (such as kinetic factors, lattice strain, or Coulombic forces, etc…). The most favourable composition can therefore only be unambiguously predicted when only one minimum occurs in the curve (as in

Figure 4, Figures 5a, 5c). Otherwise the approach needs to be combined with experiments or $ab-initio$ calculations on the set of composition corresponding to minima in order to determine the most favourable composition. Nevertheless, our neighbour analysis approach to predicting mineral composition has proven useful in describing the major phases of the Earth's interior and could have uses in determining compositions in other thermodynamic conditions. This is an important development, as experimental complications associated with phase equilibration experiments, such as sluggish kinetics of the ion exchange reactions, provide difficulties in predicting mineral composition at high pressure-temperature conditions (Nakahima et al, 2012).

Exchange interactions are important in governing mineral compositions in the weak metal, as well as Hubbard insulator minerals studied here. We suspect this is because electrons are relatively itinerant in these systems, even though spin-spin interactions may occur over a long range through super-exchange interactions. This allows the crystal to vary its spin degrees of freedom in order to accommodate the most energetically favourable composition. In other systems of higher electrical conductivity, it is possible that Coulombic interactions would have a greater control on determining optimal mineral compositions. A further understanding of the mechanism inducing the observed relation between total energy, composition and magnetic moment would require a detailed sampling of the spin-hamiltonian, using for example a Heisenberg model. However, such a study is beyond our computational capabilities with current theoretical approaches.

Our results predict a composition of 12% Fe in Bm. One major factor which is not considered in the calculations is the partitioning of Fe from Bm to other phases (in particular Pr, which is the most commonly predicted stable phase in the lower mantle, excluding Bm). However, partitioning of Fe from Bm to Pr (and other phases) would need to lower the Fe in Bm to a value of 5-8% in order to agree with experiments that predict a pyrolytic composition (Ricolleau et al 2008; Kesson et al, 1998).

Assuming that the lower mantle's modal mineralogical proportions is 80% Bm and 20% Pr, our results predict that Pr would need to contain 28-40% Fe in order to lower the Fe composition of Bm to the desired value. Noteworthy is that 20% Pr is a much higher modal proportion than most experiments would suggest, so that the required Fe composition of Pr is likely much more severe. To our knowledge, no experimental or theoretical evidence exists to support such a high Fe content in Pr. Our results are therefore consistent with a compositionally layered mantle, whereby the lower mantle adopts a more silicic (perovskitic composition). Such a chemical layering may have formed following a giant impact, such as that required for the formation of the moon. This impact would have shock melted at least a major proportion of the Earth's mantle (Frost, 2016; Canup, 2004; Carlson et al, 2014). The subsequently formed magma ocean would allow for fractional crystallization and settling of Bm, as it would have been the liquidus phase for most of the lower mantle (Frost, 2016; Adrault et al, 2011; Liebske and Frost, 2012).

The 12% Fe in Bm raises the Bm density by ~1.05% over the pure Mg end member. The actual density value also depends on the assumed unit cell volume and modal mineral proportions. However this result can help study discrepancies in model lower mantles densities compared to PREM values.

We also predict stability of more Fe rich (~0.23 Fe concentration) Bm, which provides a model to account for the presence of LLSVPs in the lower mantle (Mao et al, 2011). These anomalous Fe-rich mantle provinces may represent residues from partial melting of sinking slabs, because any extracted liquid would be buoyant and would not be preserved in the lower mantle (Andrault et al, 2012). The high Fe content can be incorporated in the Bm lattice with increased Al contents (Mao et al, 2011), and this is a probable mechanism, as subducted slabs are often highly aluminous due to the immobility of aluminous phases during metasomatism. The interpretation of LLSVPs as representing chemically distinct piles would suggest that chemical gradients exist in the lower mantle and this

provides an additional mechanism for partial melting and formation of mantle plumes.

Recent geodynamical modeling (Ballmer et al, 2015) suggests that chemical layering in the mantle is not inconsistent with whole-mantle convection. The convection allows for down-going slabs to reach the lower mantle. The presence of a component of whole-mantle convection supports the hypothesis that partial melting of down going slabs produces LLSVPs. Although, we cannot completely discount the possibility of layered mantle convection, as the convective regime is highly sensitive to the mantle density profile (Ballmer et al, 2015). Layered mantle convection allows for a greater degree of preservation of local chemical gradients at the transition zone to the lower mantle boundary, which allows for partial melting and formation of mantle plumes.

## CHAPTER 5

### References


Andrault, D., N. Bolfan-Casanova, G. Lo Nigro, M. A. Bouhifd, G. Garbarino, and M. Mezouar 2011. Solidus and Liquidus Profiles of Chondritic Mantle: Implication for Melting of the Earth Across its History. *Earth and Planetary Science Letters*. 304, 251–259.

Andrault, D., S. Petitgirard, G. Lo Nigro, J. L. Devidal, G. Veronesi, G. Garbarino, and M. Mezouar 2012. Solid-liquid Iron Partitioning in Earth's Deep Mantle. *Nature*, 487, 354–357.

Aryasetiawan, F., Karlsson, K., Jepsen, O. and Schonberger, U. 2006. Calculation of Hubbard U from First Principles. *Phys Rev. B.* 74(12), 125106-1-9.

Ballmer, M.D., Schmerr, N.C., Nakagawa, T. and Ritsema, J. 2015. Compositional Mantle Layering Revealed by Slab Stagnation at ~1000-km Depth. *Science Advances.* 1:e1500815.

Bernstein, S., Kelemen, P.B. and Hanhoj, K. 2007. Consistent Olivine Mg# in Cratonic Mantle Reflects Archean Mantle Melting to the Exhaustion of Orthopyroxene. *Geology.* 35(5), 459-462.

Blochl, P.E. 1994. Projector Augmented-Wave Method. *Phys. Rev. B.* 50(24), 17953-17979.

Canup, R. M. 2004. Simulations of a Late Lunar-forming Impact. *Icarus*. 168, 433–456.

Carlson, R. W., E. Garnero, T. M. Harrison, J. Li., M. Manga, W. F. McDonough, S. Mukhopadhyay, B. Romanowicz, D. Rubie, Zhong S. and Williams Q. 2014. How did Early Earth Become our Modern World? *Annual Review of Earth and Planetary Science*. 42, 151–178.

Casassa, S., & Ferrari, A. M. (2016). Calibration of 57 Fe Mössbauer Constants by First Principles. *Physical Chemistry Chemical Physics*. 18(15), 10201-10206.

Deuss, A., Redfern, S.A.T., Chambers, K., Woodhouse, J.H. 2006. The Nature of the 660-Kilometer Discontinuity in Earth's Mantle from Global Seismic Observations of PP Precursors. *Science.* 331, 198-201.

Dovesi, R., Orlando, R., Erba, A., Zicovich-Wilson, C.M., Civalleri, B., Casassa, S., Maschio, L., Ferrabone, M., De La Pierre, M., D'Arco, P. and Noël, Y., 2014. CRYSTAL14: A Program for the Ab Initio Investigation of Crystalline Solids. *International Journal of Quantum Chemistry*. 114(19), 1287-1317.

Duradev, S.L., Botton, G.A., Savrasov, S.Y., Humphreys, C.J. and Sutton A.P. 1998. Electron-Energy-Loss Spectra and the Structural Stability of Nickel Oxide: An LSDA+U Study. *Phys. Rev. B.* 57(3), 1505-1509.

Dziewonski, A.M. and Anderson, D.L., 1981. Preliminary Reference Earth Model. *Physics of the Earth and Planetary Interiors*. 25, 297-356.

Efthimiopoulos, I., Liu, Z.T.Y., Khare, S.V., Sarin, P., Lochbiler, T., Tsurkan, V., Loidl, A., Popov, D. and Wang, Y. 2015. Pressure-Induced Transition in the Multiferroic CoC r2O4 Spinel. *Physical Review B*. 92(6), 064108.

Fei, Y., Mao, H.K., Shu, J. and Hu, J. 1992. PVT Equation of State of Magnesiowüstite (Mg0. 6Fe0. 4) O. *Physics and Chemistry of Minerals*. 18, 416-422.

Fiquet, G., Dewaele, A., Andrault, D., Kunz, M. and Le Bihan, T. 2000. Thermoelastic Properties and Crystal structure of MgSiO3 Perovskite at Lower Mantle Pressure and Temperature Conditions. *Geophysical Research Letters*, 27, 21-24.

Frost, D., J. and Myhill R. 2016. Chemistry of the Lower Mantle. *Deep Earth: Physics and Chemistry*

*of the Lower Mantle and Core*. *In Press.*

Frost, D. J. 2008. The Upper Mantle and Transition Zone. *Elements*. 4(3), 171-176.

Frost, D. J., and F. Langenhorst. 2002. The Effect of Al2O3 on Fe-Mg Partitioning Between Magnesiowüstite and Magnesium Silicate Perovskite. *Earth Planet. Sci. Lett.* 199, 227–241, doi:10.1016/S0012-821X(02) 00558-7.

Frost, D. J., F. Langenhorst, and P. A. van Aken. 2001. Fe-Mg Partitioning Between Ringwoodite and Magnesiowüstite and the Effect of Pressure, Temperature and Oxygen Fugacity. *Phys. Chem. Miner.* 28, 455–470, doi:10.1007/s002690100181.

Harris, D.C. and Nickel, E.H. 1972. Pentlandite Compositions and Associations in Some Mineral Deposits. *Canadian Mineralogist.* 11, 861-878.

Hoffman, E., Housley, R.M., Bland, P.A., Seifu, D. and Oliver, F.W. 2001. Fe-Rich Pentlandite in Allende Bulk Sample and Separates: Mossbauer Spectroscopic Analysis. *32nd Annual Lunar and Planetary Science Conference*. March 12-16, 2001, Houston, Texas, abstract no.2116.

A W. Hofmann, 1997. Mantle Geochemistry: the Message from Oceanic Volcanism. *Nature.* 385, 219-229.

Hazen, R.M., Downs, R.T. and Finger, R.W. 1993. Crystal Chemistry of Ferromagnesian Silicate Spinels: Evidence for Mg-Si Disorder. *American Mineralogist.* 78, 1320-1323.

Hubbard, J. 1968. Electron Correlation in Narrow Energy Bands: *Proceedings of the Royal Society of London. Series A, Mathematical and Physical Sciences*. 276, 238-257

Jephcoat, A.P., Hriljac, J.A., McCammon C. A., O'Neill, H. St. C., Rubie, D.C. and Finger, R.W. 1999.

High-resolution Synchrotron X-ray Powder Diffraction and Reitvelf Structure Refinement of Two (Mg.95Fe.05)SiO3 Perovskite Samples Synthesized Under Different Oxygen Fugacity Conditions. *American Mineralogist.* 84, 214-220.

Kaminski, E. and Javoy, M. 2013. A Two-Stage Scenario for the Formation of the Earth's Mantle and Core. *Earth and Planetary Science Letters*. 365, 97-107.

Kesson, S.E., Gerald, J.F. and Shelley, J.M. 1998. Mineralogy and Dynamics of a Pyrolite Lower Mantle. *Nature*. 393, 252-255.

Kikuchi, R. 1951. Theory of Cooperative Phenomena. *Physical Review.* 81, 988-1002.

Kresse, G. and Furthmuller, J. 1996. Efficiency of Ab-Initio Total Energy Calculations for Metals and Semiconductors using a Plane-Wave Basis Set. *Computational Materials Science.* 6, 15-50.

Knop, O., Huang, C. H., Reid, K. I. G., Carlow, J. S., & Woodhams, F. W. D. 1976. Chalkogenides of the Transition Elements. X-Ray, Neutron, Mössbauer, and Magnetic Studies of Pentlandite and the π phases π (Fe, Co, Ni, S), Co 8 MS 8, and Fe 4 Ni 4 MS 8 (M= Ru, Rh, Pd). *Journal of Solid State Chemistry*. 16(1), 97-116.

Laznicka, P., 2013. Empirical metallogeny: Depositional Environments, Lithologic Associations and Metallic ores. Elsevier.

Lin, J.F., Watson, H., Vankó, G., Alp, E.E., Prakapenka, V.B., Dera, P., Struzhkin, V.V., Kubo, A., Zhao, J., McCammon, C. and Evans, W.J. 2008. Intermediate-Spin Ferrous Iron in Lowermost Mantle Post-Perovskite and Perovskite. *Nature Geoscience*. 1(10), 688-691.

Lin, J. F., Gavriliuk, A. G., Sturhahn, W., Jacobsen, S. D., Zhao, J., Lerche, M., & Hu, M. 2009. Synchrotron Mössbauer Spectroscopic Study of Ferropericlase at High Pressures and Temperatures.

*American Mineralogist*. 94(4), 594-599.

Mao, Z., Lin, J.F., Scott, H.P., Watson, H.C., Prakapenka, V.B., Xiao, Y., Chow, P. and McCammon, C. 2011. Iron-rich Perovskite in the Earth's Lower Mantle. *Earth and Planetary Science Letters*, 309, 179-184.

Marty, B. 2012. The Origins and Concentrations of Water, Carbon, Nitrogen and Noble Gases on Earth. *Earth Planetary Science Letters*. 313–314, 56–66.

Merli, M., Oberti, R., Caucia, F. and Ungaretti L. 2001. Determinations of Site Populations in Olivine: Warnings on X-ray data. *American Mineralogist.* 86, 55-65.

Moreira, M., Breddam, K., Curtice, J. and Kurz, M. 2001. Solar Neon in the Icelandic Mantle: Evidence for an Undegassed Lower Mantle. *Earth Planetary Science Letters*. 185, 15–23.

Mukhopadhyay, S. 2012. Early Differentiation and Volatile Accretion Recorded in Deep-Mantle Neon and Xenon. *Nature*. 486, 101–104.

Murakami, M., Hirose, K., Sata, N. and Ohishi, Y. 2005. Post-perovskite phase transition and mineral chemistry in the pyrolitic lowermost mantle. *Geophysical Research Letters*. 32(3), L03304-L03307.

Murakami, M., Ohishi, Y., Hirao, N. and Hirose, K. 2012. A Perovskitic Lower Mantle Inferred from High-pressure, High-temperature Sound Velocity Data. *Nature.* 482, 90-95.

Mustapha, S., D'Arco, P., De La Pierre, M., Noël, Y., Ferrabone, M., and Dovesi, R. 2013. On the Use of Symmetry in Configurational Analysis for the Simulation of Disordered Solids. *Journal of Physics: Condensed Matter*. 25(10), 105401.

Nakajima, Y., Frost, D.J. and Rubie D.C. 2012. Ferrous Iron Partitioning Between Magnesium Silicate

Perovskite and Ferropericlase and the Composition of Perovskite in the Earth's Lower Mantle. *Journal of Geophysical Research.* 117, B08201-B08212.

Nakazawa, H., Osaka, T. and Sakaguchi, K. 1973. A New Cubic Iron Sulfide Prepared by Vacuum Deposition. *Nature Physical Science.* 242, 13-14.

Nemykin, V. N. and Hadt, R. G. (2006). Influence of Hartree-Fock Exchange on the Calculated Mössbauer Isomer Shifts and Quadrupole Splittings in Ferrocene Derivatives Using Density Functional Theory. *Inorganic Chemistry*. 45(20), 8297-8307.

Ozawa, H., Hirose, K., Mitome, M., Bando Y., Sata, N. and Ohishi, Y. 2008. Chemical Equilibrium Between Ferropericlase and Molten Iron to 134 GPa and Implications for Iron Content to the Bottom of the Mantle. *Geophysical Research Letters.* 35, L05308-L05312.

Perdew, J.P., Burke, K. and Ernzerhof, M. 1996. Generalized Gradient Approximation Made Simple. *Physical Review Letter.* 78, 1396.

Ricolleau, A., Fei, Y., Cottrell, E., Watson, H., Deng, L., Zhang, L., Fiquet, G., Auzende, A.L., Roskosz, M., Morard, G. and Prakapenka, V. 2009. Density profile of Pyrolite Under the Lower Mantle Conditions. *Geophysical Research Letters*. 36(6), L06302-L06307.

Sanchez, J.M., Ducastelle, F. and Gratias, D. 1984. Generalized Cluster Description of Multicomponent Systems. *Physica*. 128A, 334-350.

Sarmiento-Pérez, R., Botti, S., Schnohr, C. S., Lauermann, I., Rubio, A., and Johnson, B. 2014. Local Versus Global Electronic Properties of Chalcopyrite Alloys: X-ray Absorption Spectroscopy and Ab Initio Calculations. *Journal of Applied Physics*. 116(9), 093703.

G. Schubert, D. L. Turcotte, P. Olsen. 2001. Mantle Convection in the Earth and Planets. Cambridge

University Press, Cambridge, UK.

Sinnecker, S., Slep, L. D., Bill, E., and Neese, F. 2005. Performance of Nonrelativistic and Quasi-Relativistic Hybrid DFT for the Prediction of Electric and Magnetic Hyperfine Parameters in 57Fe Mössbauer Spectra. *Inorganic chemistry*. 44(7), 2245-2254.

Skelton, R., and Walker, A. M. 2015. The Effect of Cation Order on the Elasticity of Omphacite from Atomistic Calculations. *Physics and Chemistry of Minerals*. 42(8), 677-691.

Tenailleau, C., Etschmann, B., Ibberson, R. M., and Pring, A. 2006. A Neutron Powder Diffraction Study of Fe and Ni Distributions in Synthetic Pentlandite and Violarite Using 60Ni Isotope. *American Mineralogist*. 91(8-9), 1442-1447.

Tschauner, O., Ma, C., Beckett, J.R., Prescher, C., Prakapenka, V.B. and Rossman, G.R. 2014. Discovery of Bridgmanite, the Most Abundant Mineral in Earth, in a Shocked Meteorite. *Science*. 346, 1100-1102.

Tsuchiya, T., Wentzcovitch, R. M., da Silva, C. R., and de Gironcoli, S. 2006. Spin Transition in Magnesiowüstite in Earth's Lower Mantle. *Physical Review Letters*. 96(19), 198501.

Van de Walle, A., Tiwary, P., de Jong, M., Olmsted, D.L., Asta, M., Dick, A., Shin, D., Wang, Y., Chen, L,-Q. and Liu, Z.-K. 2013. Efficient Stochastic Generation of Special Quasirandom Structures. *CALPHAD: Computer Coupling of Phase Diagrams and Thermochemistry.* 42, 13-18.

Van de Walle, A. 2009. Multicomponent, Multisublattice Alloys, Nonconfigurational Entropy and Other Additions to the Alloy Theoretic Automated Toolkit. *CALPHAD: Computer Coupling of Phase Diagrams and Thermochemistry.* 33, 266-278.

Yates, J. R., Pickard, C. J., and Mauri, F. 2007. Calculation of NMR Chemical Shifts for Extended

Systems Using Ultrasoft Pseudopotentials. *Physical Review B*. 76(2), 024401.

Zhang, L., Meng, Y., Yang, W., Wang, L., Mao, W.L., Zeng, Q.S., Jeong, J.S., Wagner, A.J., Mkhoyan, K.A., Liu, W. and Xu, R. 2014. Disproportionation of (Mg, Fe) SiO3 Perovskite in Earth's Deep Lower Mantle. *Science*. 344, 877-882.

# Chapter 6

# APPENDIX I

# Supplementary Information

## 6.1 The SQS Calculation

In all SQS calculations reported, we test the convergence of the solutions with respect to supercell size, number of matched cluster functions and by assuring that a global minimum is reached in the minimization through increasing the fictitious simulated annealing temperature. As in Pn, we assume that the solutions have converged when 12 independent samplings of $Q$ reach the same result and we use the weight $\omega = 1$. We report the obtained absolute values of the correlation differences in Tables S1-S7. The correlations are for specific cluster functions, which are labelled by two indices $i, j$ in $\Delta\rho_{i,j}$, where $i$ denotes the number of lattice sites and $j$ denotes the number of nearest neighbor shells. When results are presented in the thesis for the same mineral at different pressures or temperatures, we performed the calculations individually on all lattices. However, sometimes we found no difference in the obtained correlation differences, so we only report the correlation differences for one representative calculation. For the Pr calculations, we used a 3*1*1 supercell consisting of 60 atoms. 2-body correlations were matched up to sixth nearest neighbor, while three- and four-body correlations were matched up to second nearest neighbor. For the Bm calculations at 25 GPa, we used a 3*4*2 supercell consisting of 480 atoms. Two-body correlations were matched up to seventh nearest neighbor, while three-body correlations were matched up to fifth nearest neighbor and four-body correlation were matched up to sixth nearest neighbor. Fot the Bm calculations at ~100 GPa, we used a 3*4*4 supercell consisting of 960 atoms. Two and three body correlations were matched up to fifth nearest neighbour. For Rw, we used a 5*1*1 supercell consisting of 70 atoms. 2-body correlations were matched up to

fifth nearest neighbor, while three- and four-body correlations were matched up to second nearest neighbor. Finally for Ol, we used a 3*1*2 supercell consisting of 168 atoms. 2-body correlations were matched up to sixth nearest neighbor, while three body correlations were matched up to third nearest neighbor and four-body correlations were matched up to seventh nearest neighbor shells.

### 6.2 Pn *Ab-initio* Calculations

The AE/HSE calculations were performed using a Γ-centered 4*4*4 mesh in the reciprocal net and an 8*8*8 mesh in the Gilat net. We use a Fermi finite-temperature smearing of the fermi-surface, using the smearing width $kT = 0.02\ ha$ and the spin-unrestricted formalism. For Fe and Ni, we use the 86-411(d41)G basis sets of Towler et al (1995). For S, we use the 86-3111G** basis set of Bredow et al (2004). These basis sets consist of a set of Gaussian functions. The Gaussian functions are grouped (or contracted) into so-called shells for the purposes of evaluating bielectronic integrals (see below). The Gaussian with the lowest exponent is called the adjoined Gaussian of the shell. The Gaussian functions are combined linearly to form the so-called atomic-orbitals, which are approximations to Slater functions. The atomic-orbitals have the same periodicity as the crystal. A linear combination of atomic-orbitals multiplied by plane waves forms a Bloch function. The Bloch functions offer a convenient way to capture the effects of the periodicity of the (infinite) crystal on the electronic wavefunction at any point in space. A linear combination of Bloch functions provides a basis for representing the electronic wavefunction of the infinite crystal.

Finally, Treatment of integrals related to the Coulomb and Exchange series are controlled in the CRYSTAL14 code using five parameters which were set to 6 6 6 6 12. The first parameter is $ITOL1 = -log_{10}S_c$ and Coulomb integrals are disregarded if the total charge of the relevant atomic-orbital is smaller than $S_c$. A similar (the third) parameter $ITOL3$ is defined for the Exchange integrals. The second parameter is $ITOL2 = -log_{10}S_{1\lambda}$ and classifies Coulomb integrals by a comparison of $S_{1\lambda}$ to the value of the overlap integrals between shells of contracted Gaussians. The contractions are implemented in the definition of the basis-set (see above). The overlap integrals of the shells are evaluated using the adjoined Gaussian of the respective shells. Classification of the Coulomb integrals means that they are either assigned to the exact, short-range or long-range zones. In the exact zone,

Coulomb integrals are fully evaluated using an analytical formula. In the short-range zone, Coulomb integrals are evaluated through a multipolar expansion. In the long-range zone, Coulomb integrals are evaluated using Ewald's method combined with recursion formulae. The fourth and fifth parameters $ITOL4$ and $ITOL5$ are used to disregard Exchange integrals (smaller than $10^{-ITOL4}$ or $10^{-ITOL5}$) involving atomic-orbitals belonging to adjoining cells (see Dovesi et al, 2014 and references therein).

### 6.3 Pr Ab-initio Calculations

The Pr calculations were performed using an identical functional to that for Pn. We adopted a Γ-centered 2*2*6 net for sampling reciprocal space and a 400 eV plane-wave energy-cutoff, as well as convergence criteria for the electronic and ionic SCF loops. The PBE/PAW potentials of Kresse and Joubert (1999) were used. For Fe, semi-core s and semi-core p states, as well as d electrons are treated as valence states. For Mg and O, semi-core s and semi-core p states were treated as valence states. The total magnetic moments of Figure 6 were calculated using a tighter tolerance of 500 eV for the plane-wave energy cutoff and electronic loop convergence criteria.

## 6.4 Supplementary Tables

**Table S1. Pn First Mixing Model Correlation Differences**

| Fe/(Fe+Ni) | $\Delta\rho_{2,2}$ | $\Delta\rho_{2,3}$ | $\Delta\rho_{2,4}$ | $\Delta\rho_{2,5}$ | $\Delta\rho_{2,6}$ | $\Delta\rho_{2,7}$ | $\Delta\rho_{3,3}$ | $\Delta\rho_{4,3}$ |
|---|---|---|---|---|---|---|---|---|
| 0.1111111 | 0.020833 | 0.020833 | 0.020833 | 0.020833 | -0.0625 | 0 | 0.078125 | 0.183594 |
| 0.2222222 | 0 | -0.08333 | 0 | 0 | 0 | 0 | -0.125 | -0.0625 |
| 0.3333333 | -0.0625 | -0.0625 | 0.020833 | 0.020833 | -0.0625 | 0 | -0.01563 | -0.00391 |
| 0.4444444 | 0 | -0.16667 | 0 | 0 | 0 | 0 | 0 | 0 |
| 0.5 | 0 | -0.16667 | 0 | 0 | 0 | 0 | 0 | 0 |
| 0.5555556 | 0 | -0.16667 | 0 | 0 | 0 | 0 | 0 | 0 |
| 0.6111111 | 0.067708 | -0.01563 | -0.01563 | -0.0156 | -0.0156 | 0.0052 | -0.12305 | -0.00024 |
| 0.6666667 | 0.020833 | -0.0625 | -0.0625 | 0.020833 | -0.0625 | 0 | 0.015625 | -0.00391 |
| 0.7222222 | 0.026042 | 0.026042 | 0.026042 | 0.026042 | 0.10937 | 0.0052 | -0.07227 | -0.01978 |
| 0.7777778 | 0 | -0.08333 | 0 | 0 | 0 | 0 | 0.125 | -0.0625 |
| 0.8888889 | 0.020833 | 0.020833 | 0.020833 | 0.020833 | -0.0625 | 0 | -0.07813 | 0.183594 |

**Table S2. Pn Second Mixing Model Correlation Differences**

| Fe/(Fe+Ni) | $\Delta\rho_{2,2}$ | $\Delta\rho_{2,3}$ | $\Delta\rho_{2,4}$ | $\Delta\rho_{2,5}$ | $\Delta\rho_{2,6}$ | $\Delta\rho_{2,7}$ | $\Delta\rho_{3,3}$ | $\Delta\rho_{4,3}$ |
|---|---|---|---|---|---|---|---|---|
| 0.1111111 | 0.020833 | 0.020833 | 0.020833 | 0.020833 | -0.0625 | 0 | 0.078125 | 0.183594 |
| 0.2222222 | -0.02474 | -0.02474 | -0.02474 | 0.010417 | -0.0247 | 0.05859 | 0.009521 | 0.149887 |
| 0.3333333 | 0.027344 | -0.05599 | 0.027344 | 0.010417 | 0.0273 | 0.02734 | -0.09302 | -0.25954 |
| 0.4444444 | -0.01563 | -0.01563 | 0.067708 | 0 | -0.0156 | -0.0156 | 0.123047 | -0.00024 |
| 0.5 | 0 | -0.16667 | 0 | 0 | 0 | 0 | 0 | 0 |
| 0.5555556 | -0.01563 | -0.01563 | 0.067708 | 0 | -0.0156 | -0.0156 | -0.12305 | -0.00024 |
| 0.6111111 | 0.020833 | -0.0625 | -0.0625 | 0 | 0.0208 | -0.0625 | 0.015625 | -0.00391 |
| 0.6666667 | 0.026042 | 0.026042 | 0.026042 | 0 | 0.0260 | 0.10937 | -0.07227 | -0.01978 |
| 0.7222222 | 0.016927 | -0.06641 | 0.016927 | 0.010417 | 0.0169 | -0.0664 | 0.02124 | 0.213364 |
| 0.7777778 | -0.01432 | -0.01432 | -0.01432 | 0.010417 | -0.0143 | -0.0976 | 0.012451 | 0.026596 |
| 0.8888889 | 0.020833 | 0.020833 | 0.020833 | 0.020833 | -0.0625 | 0 | 0.078125 | 0.183594 |

**Table S3. Pr Correlation Differences**

| Fe/(Fe+Mg) | $\Delta\rho_{2,2}$ | $\Delta\rho_{2,3}$ | $\Delta\rho_{2,4}$ | $\Delta\rho_{2,5}$ | $\Delta\rho_{2,6}$ | $\Delta\rho_{3,2}$ | $\Delta\rho_{4,2}$ |
|---|---|---|---|---|---|---|---|
| 0.1 | 0.004444 | 0.004444 | -0.00667 | 0.026667 | 0.004444 | -0.02133 | 0.057067 |
| 0.15 | 0.006667 | 0.04 | -0.01 | 0.24 | -0.02667 | 0.034 | 0.0704 |
| 0.2 | -0.00444 | 0.017778 | -0.01556 | -0.00444 | -0.00444 | -0.01733 | 0.0704 |
| 0.3 | 0.017778 | -0.00444 | -0.00444 | -0.00444 | 0.006667 | 0.002667 | 0.041067 |
| 0.3333333 | 0.01 | -0.09 | 0.01 | 0.21 | 0.01 | -0.027 | -0.0081 |
| 0.4 | 0.004444 | 0.026667 | 0.004444 | 0.004444 | -0.00667 | 0.008 | 0.065067 |
| 0.5 | 0 | -0.02222 | -0.01111 | 0 | 0.011111 | 0 | 0.066667 |
| 0.6 | 0.004444 | 0.026667 | -0.00667 | 0.004444 | 0.004444 | -0.008 | 0.065067 |
| 0.7 | 0.017778 | -0.00444 | -0.00444 | -0.00444 | 0.006667 | 0.002667 | 0.041067 |
| 0.75 | -0.01667 | -0.05 | -0.01667 | 0.25 | -0.01667 | -0.025 | -0.0625 |
| 0.8 | -0.00444 | 0.017778 | -0.01556 | -0.00444 | -0.00444 | 0.017333 | 0.0704 |
| 0.9 | 0.004444 | 0.004444 | -0.00667 | 0.026667 | 0.004444 | 0.021333 | 0.057067 |

**Table S4. Rw Correlation Differences**

| Fe/(Fe+Mg) | $\Delta\rho_{2,2}$ | $\Delta\rho_{2,3}$ | $\Delta\rho_{2,4}$ | $\Delta\rho_{2,4}$ | $\Delta\rho_{2,5}$ | $\Delta\rho_{3,2}$ | $\Delta\rho_{4,2}$ |
|---|---|---|---|---|---|---|---|
| 0.1 | 0.026667 | 0.026667 | 0.226667 | 0.093333 | 0.026667 | 0.088 | 0.1904 |
| 0.15 | -0.02333 | -0.02333 | 0.243333 | 0.176667 | -0.02333 | -0.043 | -0.0401 |
| 0.2 | -0.02667 | 0.006667 | 0.24 | 0.24 | 0.04 | -0.016 | 0.0704 |
| 0.3 | -0.02667 | 0.006667 | 0.306667 | 0.173333 | 0.04 | -0.064 | -0.2256 |
| 0.4 | -0.04 | -0.00667 | 0.16 | 0.16 | 0.026667 | -0.008 | -0.2016 |
| 0.5 | 0.066667 | 0 | 0.2 | 0.2 | -0.066667 | 0 | 0.2 |
| 0.6 | -0.04 | -0.00667 | 0.16 | 0.16 | 0.0266667 | 0.008 | -0.2016 |
| 0.7 | -0.02667 | 0.00667 | 0.306667 | 0.173333 | 0.04 | 0.064 | -0.2256 |
| 0.8 | -0.02667 | 0.006667 | 0.373333 | 0.106667 | 0.04 | 0.016 | 0.0704 |
| 0.9 | 0.026667 | 0.026667 | 0.226667 | 0.093333 | 0.026667 | -0.088 | 0.1904 |

**Table S5. Ol Correlation Differences**

| Fe/(Fe+Mg) | $\Delta\rho_{2,2}$ | $\Delta\rho_{2,3}$ | $\Delta\rho_{2,4}$ | $\Delta\rho_{2,5}$ | $\Delta\rho_{2,6}$ | $\Delta\rho_{3,3}$ | $\Delta\rho_{4,7}$ | $\Delta\rho_{4,7}$ | $\Delta\rho_{4,7}$ |
|---|---|---|---|---|---|---|---|---|---|
| 0.0833333 | -0.028 | -0.028 | -0.028 | -0.028 | -0.028 | 0.0787 | 0.0177 | 0.0177 | 0.0177 |
| 0.125 | -0.0625 | 0.0208 | 0.0208 | 0.0208 | 0.0208 | 0.0052 | 0.0169 | 0.0169 | 0.0169 |
| 0.1666667 | 0.0556 | -0.028 | -0.028 | -0.028 | -0.028 | -0.0370 | -0.0308 | -0.0308 | -0.0308 |
| 0.2083333 | -0.0069 | 0.0069 | -0.0069 | -0.0069 | -0.0069 | -0.0515 | -0.0324 | -0.0324 | -0.0324 |
| 0.25 | -0.0833 | 0 | 0 | 0 | 0 | -0.0417 | 0.0208 | 0.0208 | 0.0208 |
| 0.3333333 | 0.0556 | -0.028 | -0.028 | -0.028 | -0.028 | 0.0370 | -0.0123 | -0.0123 | -0.0123 |
| 0.5 | 0 | 0 | 0 | 0 | 0 | 0 | 0 | 0 | 0 |
| 0.6666667 | 0.0556 | -0.028 | -0.028 | -0.028 | -0.028 | 0.0370 | -0.0123 | -0.0123 | -0.0123 |
| 0.8333333 | 0.0556 | -0.028 | -0.028 | -0.028 | -0.028 | -0.0370 | -0.0308 | -0.0308 | -0.0308 |
| 0.9166667 | -0.028 | -0.028 | -0.028 | -0.028 | -0.028 | 0.0787 | 0.0177 | 0.0177 | 0.0177 |

**Table S6. Bm 25 GPa Correlation Differences**

| Fe/(Fe+Mg) | $\Delta\rho_{2,2}$ | $\Delta\rho_{2,3}$ | $\Delta\rho_{2,4}$ | $\Delta\rho_{2,5}$ | $\Delta\rho_{2,6}$ | $\Delta\rho_{2,7}$ | $\Delta\rho_{3,5}$ | $\Delta\rho_{3,5}$ | $\Delta\rho_{4,6}$ |
|---|---|---|---|---|---|---|---|---|---|
| 0.0625 | 0.01563 | 0.01563 | 0.01563 | 0.02604 | 0.01563 | 0.01563 | 0.00326 | 0.00326 | 0.00285 |
| 0.0833 | 0.01389 | 0.01389 | 0.01389 | 0.01389 | 0.01389 | 0.01389 | 0.00463 | 0.00463 | 0.02392 |
| 0.1042 | 0.00174 | 0.00174 | 0.00174 | 0.00174 | 0.00174 | 0.00174 | 0.00383 | 0.00383 | 0.01780 |
| 0.1250 | 0.02083 | 0.02083 | 0.02083 | 0.00000 | 0.02083 | 0.02083 | 0.01563 | 0.01563 | 0.01693 |
| 0.1458 | 0.00174 | 0.00174 | 0.00174 | 0.01910 | 0.00174 | 0.00174 | 0.00123 | 0.00123 | 0.00174 |
| 0.1667 | 0.01389 | 0.01389 | 0.01389 | 0.01389 | 0.01389 | 0.01389 | 0.00463 | 0.00463 | 0.01080 |
| 0.1875 | 0.01563 | 0.01563 | 0.01563 | 0.01563 | 0.01563 | 0.01563 | 0.00586 | 0.00586 | 0.01408 |
| 0.2083 | 0.00695 | 0.00695 | 0.00695 | 0.00695 | 0.00695 | 0.00695 | 0.00984 | 0.00984 | 0.00921 |
| 0.2292 | 0.00174 | 0.00174 | 0.00174 | 0.00174 | 0.00174 | 0.00174 | 0.00774 | 0.00774 | 0.00275 |
| 0.2500 | 0.00000 | 0.00000 | 0.00000 | 0.00000 | 0.00000 | 0.00000 | 0.00000 | 0.00000 | 0.02083 |
| 0.2708 | 0.00174 | 0.00174 | 0.00174 | 0.00174 | 0.00174 | 0.00174 | 0.01295 | 0.01295 | 0.00246 |
| 0.3125 | 0.01563 | 0.01563 | 0.01563 | 0.00521 | 0.01563 | 0.01563 | 0.00977 | 0.00977 | 0.01978 |
| 0.3750 | 0.02084 | 0.02084 | 0.02084 | 0.00000 | 0.02084 | 0.02084 | 0.00521 | 0.00521 | 0.00391 |
| 0.4375 | 0.01563 | 0.01563 | 0.01563 | 0.01563 | 0.01563 | 0.01563 | 0.00195 | 0.00195 | 0.00024 |
| 0.5000 | 0.00000 | 0.00000 | 0.00000 | 0.00000 | 0.00000 | 0.00000 | 0.00000 | 0.00000 | 0.00000 |
| 0.5625 | 0.01563 | 0.01563 | 0.01563 | 0.01563 | 0.01563 | 0.01563 | 0.00195 | 0.00195 | 0.00024 |
| 0.6250 | 0.02083 | 0.02083 | 0.02083 | 0.00000 | 0.02083 | 0.02083 | 0.00521 | 0.00521 | 0.00391 |
| 0.6875 | 0.01563 | 0.01563 | 0.01563 | 0.00521 | 0.01563 | 0.01563 | 0.00977 | 0.00977 | 0.01978 |
| 0.7500 | 0.00000 | 0.00000 | 0.00000 | 0.00000 | 0.00000 | 0.00000 | 0.00000 | 0.00000 | 0.02083 |
| 0.8125 | 0.01563 | 0.01563 | 0.01563 | 0.01563 | 0.01563 | 0.01563 | 0.00586 | 0.00586 | 0.01408 |
| 0.8750 | 0.02083 | 0.02083 | 0.02083 | 0.00000 | 0.02083 | 0.02083 | 0.01563 | 0.01563 | 0.01693 |

**Table S7. Bm 100 GPa Correlation Differences**

| Fe/(Fe+Mg) | $\Delta\rho_{2,2}$ | $\Delta\rho_{2,3}$ | $\Delta\rho_{2,4}$ | $\Delta\rho_{2,5}$ | $\Delta\rho_{3,5}$ | $\Delta\rho_{3,5}$ |
|---|---|---|---|---|---|---|
| 0.0417 | 0.006944 | 0.006944 | 0.006944 | 0.013889 | 0.000579 | 0.000579 |
| 0.0625 | 0.005208 | 0.005208 | 0.005208 | 0.005208 | 0.003255 | 0.003255 |
| 0.0833 | 0.006944 | 0.006944 | 0.006944 | 0.003472 | 0.005787 | 0.005787 |
| 0.1042 | 0.001736 | 0.001736 | 0.001736 | 0.001736 | 0.003834 | 0.003834 |
| 0.1250 | 0.000000 | 0.000000 | 0.000000 | 0.000000 | 0.005208 | 0.005208 |
| 0.1458 | 0.001736 | 0.001736 | 0.001736 | 0.001736 | 0.001230 | 0.001230 |
| 0.1667 | 0.006944 | 0.006944 | 0.006944 | 0.003472 | 0.005787 | 0.005787 |
| 0.1875 | 0.005208 | 0.005208 | 0.005208 | 0.005208 | 0.004557 | 0.004557 |
| 0.2083 | 0.006944 | 0.006944 | 0.006944 | 0.003472 | 0.000579 | 0.000579 |
| 0.2292 | 0.001736 | 0.001736 | 0.001736 | 0.008681 | 0.002677 | 0.002677 |
| 0.2500 | 0.000000 | 0.000000 | 0.000000 | 0.000000 | 0.000000 | 0.000000 |
| 0.2917 | 0.006944 | 0.006944 | 0.006944 | 0.003472 | 0.000579 | 0.000579 |
| 0.3333 | 0.006944 | 0.006944 | 0.006944 | 0.003472 | 0.005787 | 0.005787 |
| 0.3750 | 0.000000 | 0.000000 | 0.000000 | 0.000000 | 0.005208 | 0.005208 |
| 0.4167 | 0.006944 | 0.006944 | 0.006944 | 0.003472 | 0.005787 | 0.005787 |
| 0.5000 | 0.000000 | 0.000000 | 0.000000 | 0.000000 | 0.000000 | 0.000000 |
| 0.6250 | 0.000000 | 0.000000 | 0.000000 | 0.010417 | 0.036458 | 0.005208 |
| 0.7500 | 0.000000 | 0.000000 | 0.000000 | 0.000000 | 0.000000 | 0.000000 |
| 0.8750 | 0.000000 | 0.000000 | 0.000000 | 0.000000 | 0.005208 | 0.005208 |

## 6.5 Supplementary Figures

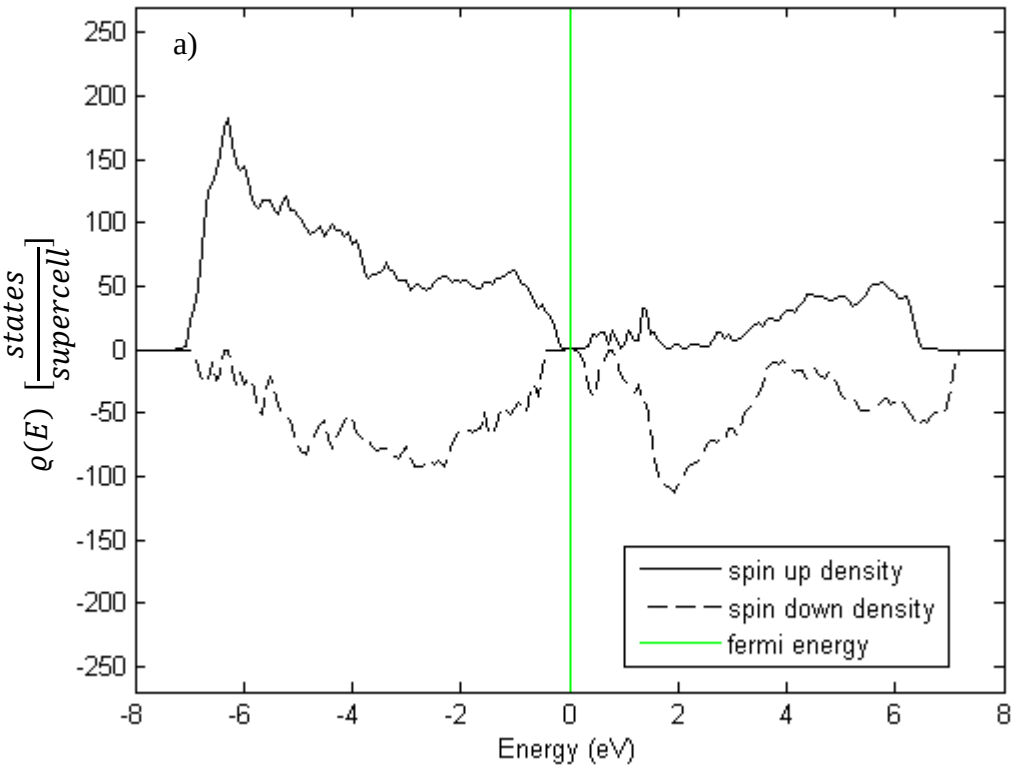


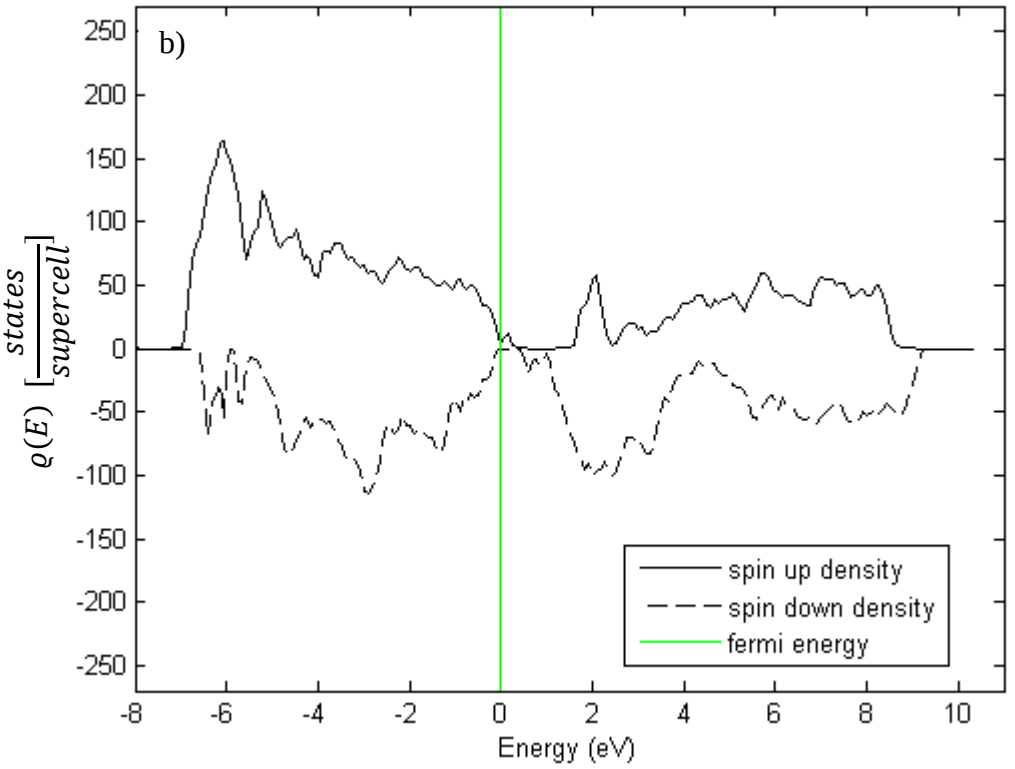

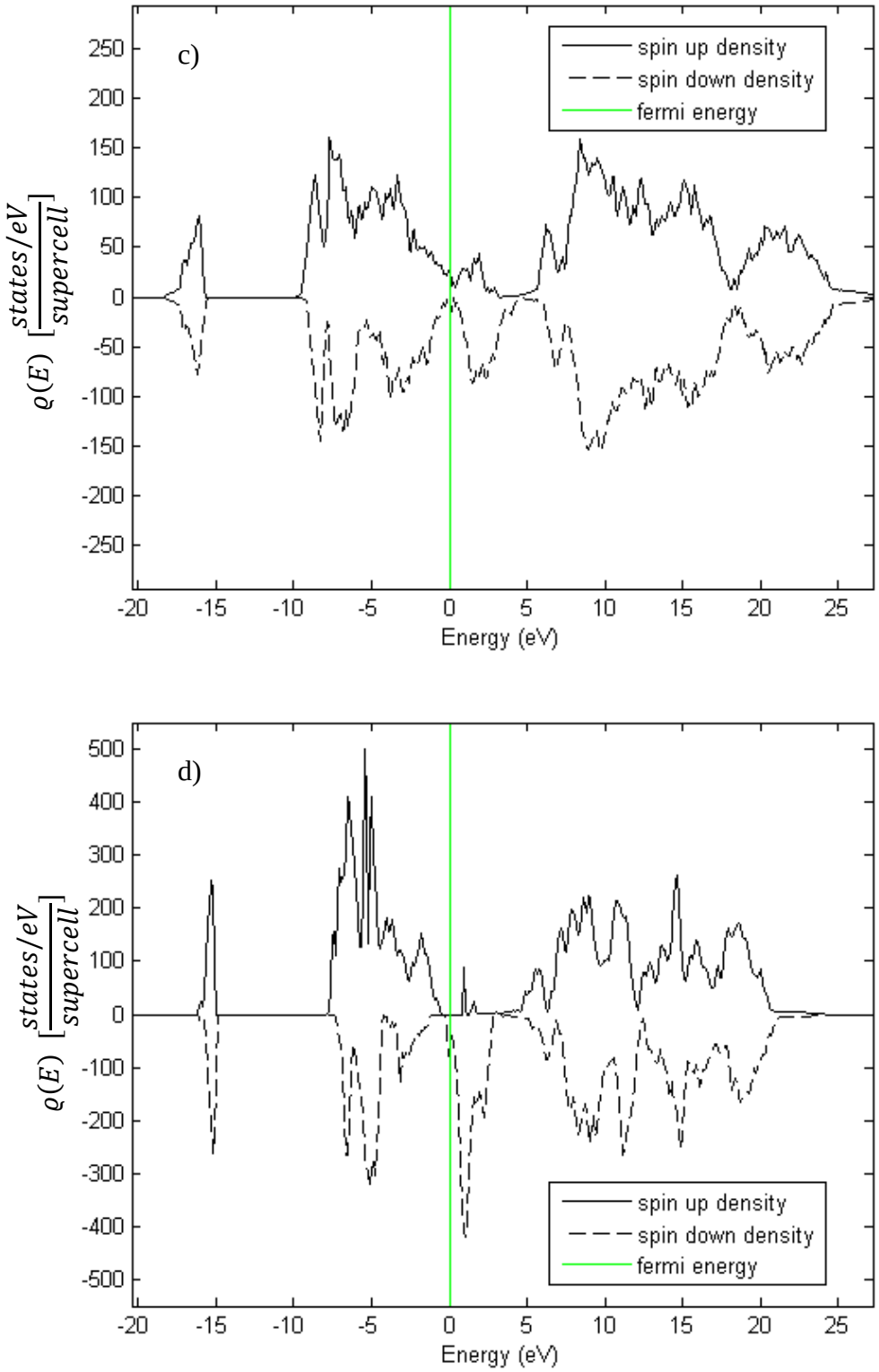


**Figure S1**: Total density of states in the energy scale for (a) Terrestrial Pn and (b) Extraterrestrial Pn with PAW/GGA+U and similar plots for (c) Terrestrial Pn and (b) Extraterrestrial Pn with HSE.

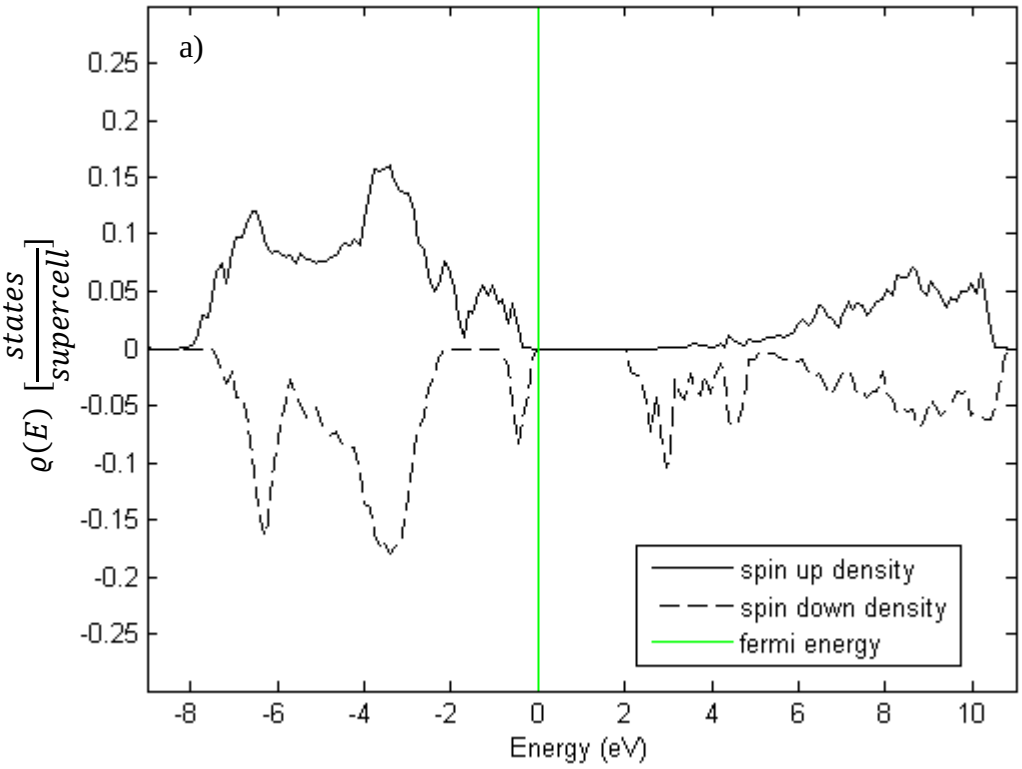
a)
0.25
0.2
0.15
0.1
0.05
0
-0.05
-0.1
-0.15
-0.2
-0.25
$\varrho(E)\ [\frac{states}{supercell}]$
-8
-6
-4
-2
0
2
4
6
8
10
Energy (eV)
spin up density
spin down density
fermi energy

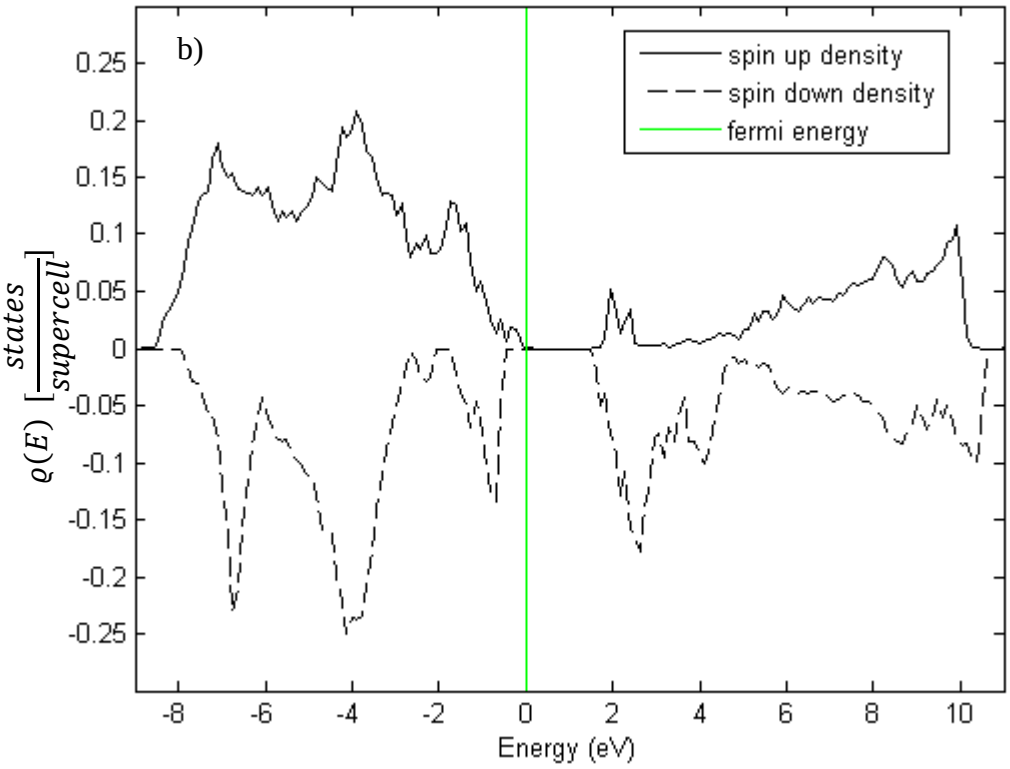
b)
0.25
0.2
0.15
0.1
0.05
0
-0.05
-0.1
-0.15
-0.2
-0.25
$\varrho(E)\ [\frac{states}{supercell}]$
-8
-6
-4
-2
0
2
4
6
8
10
Energy (eV)
spin up density
spin down density
fermi energy

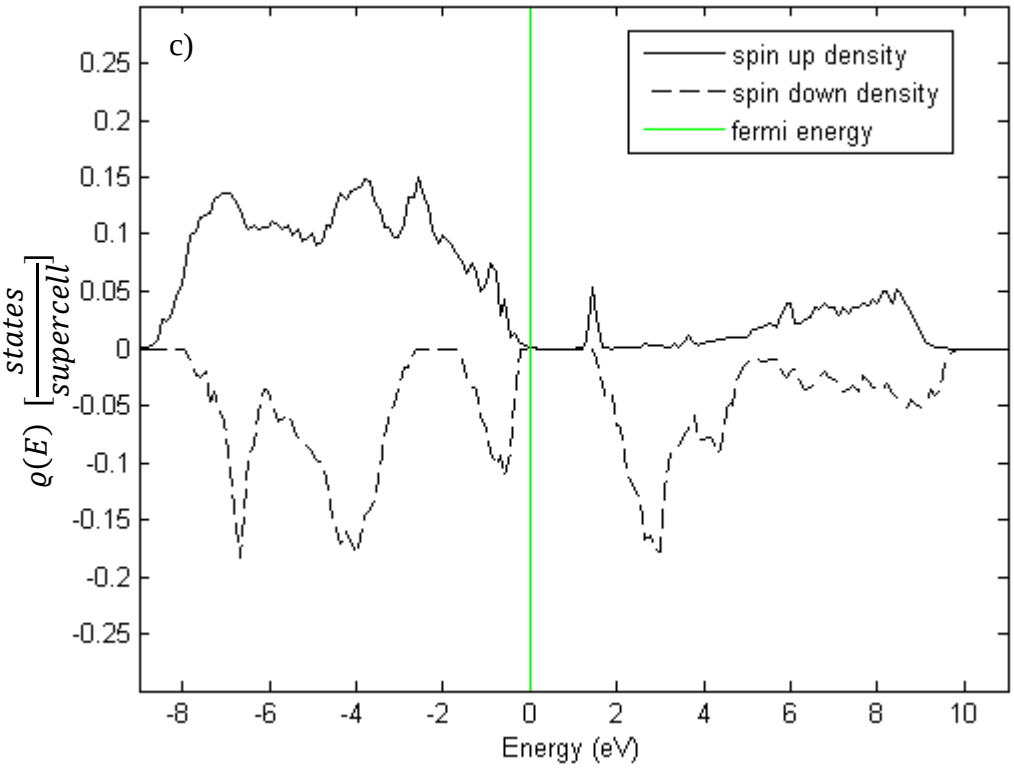


**Figure S2**: Total density of states in the energy scale for Pr with an Fe concentration of (a) 0.2 (b) 0.35 and (c) 0.5.

**Supplementary References:**

Blaha, P. and Schwarz, K. 1988. Theoretical Investigation of Isomer Shifts in Fe, FeAl, FeTi and FeCo. *Journal de Physique* 49(12), C8-101 – C8102.

Bredow T., Heitjans P., Wilkening M. 2004. Electric field gradient Calculations for LixTiS2 and Comparison with Li-7 NMR Results. *Phys. Rev. B* 70, 15111.

Dufek, P., Blaha, P. and Schwarz, K. 1995. Determination of the Nuclear Quadrupole Moment of 57 Fe. *Physical Review Letters 75*(19), 3545.

Kresse, G. and Joubert D. 1999. From Ultrasoft Pseudopotentials to the Projector Augmented-Wave Method. *Physical Review B* 59(3), 1758-1775.

Towler, M.D., Dovesi, R. and Saunders, V.R. 1995. Magnetic Interactions and the Cooperative Jahn-Teller Effect in KCuF3. *Physical Review B.* 52(14), 10150-10160

## Chapter 7

## APPENDIX II

### Example Neighbour Analysis MATLAB Code

```
pos_Fe2=xlsread('C:\Users\Jacques.JacquesDesmarai\bm_sqs_100GPa\Fe2.xlsx','E7:G198');
pos_Fe3=xlsread('C:\Users\Jacques.JacquesDesmarai\bm_sqs_100GPa\Fe3.xlsx','E7:G198');
pos_Fe4=xlsread('C:\Users\Jacques.JacquesDesmarai\bm_sqs_100GPa\Fe4.xlsx','E7:G198');
pos_Fe5=xlsread('C:\Users\Jacques.JacquesDesmarai\bm_sqs_100GPa\Fe5.xlsx','E7:G198');
pos_Fe6=xlsread('C:\Users\Jacques.JacquesDesmarai\bm_sqs_100GPa\Fe6.xlsx','E7:G198');
pos_Fe7=xlsread('C:\Users\Jacques.JacquesDesmarai\bm_sqs_100GPa\Fe7.xlsx','E7:G198');
pos_Fe8=xlsread('C:\Users\Jacques.JacquesDesmarai\bm_sqs_100GPa\Fe8.xlsx','E7:G198');
pos_Fe9=xlsread('C:\Users\Jacques.JacquesDesmarai\bm_sqs_100GPa\Fe9.xlsx','E7:G198');
pos_Fe10=xlsread('C:\Users\Jacques.JacquesDesmarai\bm_sqs_100GPa\Fe10.xlsx','E7:G198');
pos_Fe11=xlsread('C:\Users\Jacques.JacquesDesmarai\bm_sqs_100GPa\Fe11.xlsx','E7:G198');
pos_Fe12=xlsread('C:\Users\Jacques.JacquesDesmarai\bm_sqs_100GPa\Fe12.xlsx','E7:G198');
pos_Fe13=xlsread('C:\Users\Jacques.JacquesDesmarai\bm_sqs_100GPa\Fe13.xlsx','E7:G198');
pos_Fe14=xlsread('C:\Users\Jacques.JacquesDesmarai\bm_sqs_100GPa\Fe14.xlsx','E7:G198');
pos_Fe16=xlsread('C:\Users\Jacques.JacquesDesmarai\bm_sqs_100GPa\Fe16.xlsx','E7:G198');
pos_Fe18=xlsread('C:\Users\Jacques.JacquesDesmarai\bm_sqs_100GPa\Fe18.xlsx','E7:G198');
pos_Fe20=xlsread('C:\Users\Jacques.JacquesDesmarai\bm_sqs_100GPa\Fe20.xlsx','E7:G198');
pos_Fe24=xlsread('C:\Users\Jacques.JacquesDesmarai\bm_sqs_100GPa\Fe24.xlsx','E7:G198');
pos_Fe30=xlsread('C:\Users\Jacques.JacquesDesmarai\bm_sqs_100GPa\Fe30.xlsx','E7:G198');
pos_Fe36=xlsread('C:\Users\Jacques.JacquesDesmarai\bm_sqs_100GPa\Fe36.xlsx','E7:G198');
pos_Fe42=xlsread('C:\Users\Jacques.JacquesDesmarai\bm_sqs_100GPa\Fe42.xlsx','E7:G198');
pos_Fe2=transpose(pos_Fe2);
pos_Fe3=transpose(pos_Fe3);
pos_Fe4=transpose(pos_Fe4);
pos_Fe5=transpose(pos_Fe5);
pos_Fe6=transpose(pos_Fe6);
pos_Fe7=transpose(pos_Fe7);
```

```
pos_Fe8=transpose(pos_Fe8);
pos_Fe9=transpose(pos_Fe9);
pos_Fe10=transpose(pos_Fe10);
pos_Fe11=transpose(pos_Fe11);
pos_Fe12=transpose(pos_Fe12);
pos_Fe13=transpose(pos_Fe13);
pos_Fe14=transpose(pos_Fe14);
pos_Fe16=transpose(pos_Fe16);
pos_Fe18=transpose(pos_Fe18);
pos_Fe20=transpose(pos_Fe20);
pos_Fe24=transpose(pos_Fe24);
pos_Fe30=transpose(pos_Fe30);
pos_Fe36=transpose(pos_Fe36);
pos_Fe42=transpose(pos_Fe42);
bond_2=zeros(192,192);
bond_3=zeros(192,192);
bond_4=zeros(192,192);
bond_5=zeros(192,192);
bond_6=zeros(192,192);
bond_7=zeros(192,192);
bond_8=zeros(192,192);
bond_9=zeros(192,192);
bond_10=zeros(192,192);
bond_11=zeros(192,192);
bond_12=zeros(192,192);
bond_13=zeros(192,192);
bond_14=zeros(192,192);
bond_16=zeros(192,192);
bond_18=zeros(192,192);
bond_24=zeros(192,192);
```

```
bond_30=zeros(192,192);
bond_36=zeros(192,192);
bond_42=zeros(192,192);
for i=1:192
   for j=1:192
      bond_2(i,j)=sqrt((pos_Fe2(1,i)-pos_Fe2(1,j))^2+(pos_Fe2(2,i)-pos_Fe2(2,j))^2+(pos_Fe2(3,i)-
pos_Fe2(3,j))^2);
      bond_3(i,j)=sqrt((pos_Fe3(1,i)-pos_Fe3(1,j))^2+(pos_Fe3(2,i)-pos_Fe3(2,j))^2+(pos_Fe3(3,i)-
pos_Fe3(3,j))^2);
      bond_4(i,j)=sqrt((pos_Fe4(1,i)-pos_Fe4(1,j))^2+(pos_Fe4(2,i)-pos_Fe4(2,j))^2+(pos_Fe4(3,i)-
pos_Fe4(3,j))^2);
      bond_5(i,j)=sqrt((pos_Fe5(1,i)-pos_Fe5(1,j))^2+(pos_Fe5(2,i)-pos_Fe5(2,j))^2+(pos_Fe5(3,i)-
pos_Fe5(3,j))^2);
      bond_6(i,j)=sqrt((pos_Fe6(1,i)-pos_Fe6(1,j))^2+(pos_Fe6(2,i)-pos_Fe6(2,j))^2+(pos_Fe6(3,i)-
pos_Fe6(3,j))^2);
      bond_7(i,j)=sqrt((pos_Fe7(1,i)-pos_Fe7(1,j))^2+(pos_Fe7(2,i)-pos_Fe7(2,j))^2+(pos_Fe7(3,i)-
pos_Fe7(3,j))^2);
      bond_8(i,j)=sqrt((pos_Fe8(1,i)-pos_Fe8(1,j))^2+(pos_Fe8(2,i)-pos_Fe8(2,j))^2+(pos_Fe8(3,i)-
pos_Fe8(3,j))^2);
      bond_9(i,j)=sqrt((pos_Fe9(1,i)-pos_Fe9(1,j))^2+(pos_Fe9(2,i)-pos_Fe9(2,j))^2+(pos_Fe9(3,i)-
pos_Fe9(3,j))^2);
      bond_10(i,j)=sqrt((pos_Fe10(1,i)-pos_Fe10(1,j))^2+(pos_Fe10(2,i)-
pos_Fe10(2,j))^2+(pos_Fe10(3,i)-pos_Fe10(3,j))^2);
      bond_11(i,j)=sqrt((pos_Fe11(1,i)-pos_Fe11(1,j))^2+(pos_Fe11(2,i)-
pos_Fe11(2,j))^2+(pos_Fe11(3,i)-pos_Fe11(3,j))^2);
      bond_12(i,j)=sqrt((pos_Fe12(1,i)-pos_Fe12(1,j))^2+(pos_Fe12(2,i)-
pos_Fe12(2,j))^2+(pos_Fe12(3,i)-pos_Fe12(3,j))^2);
      bond_13(i,j)=sqrt((pos_Fe13(1,i)-pos_Fe13(1,j))^2+(pos_Fe13(2,i)-
pos_Fe13(2,j))^2+(pos_Fe13(3,i)-pos_Fe13(3,j))^2);
      bond_14(i,j)=sqrt((pos_Fe14(1,i)-pos_Fe14(1,j))^2+(pos_Fe14(2,i)-
```

```
pos_Fe14(2,j))^2+(pos_Fe14(3,i)-pos_Fe14(3,j))^2);
      bond_16(i,j)=sqrt((pos_Fe16(1,i)-pos_Fe16(1,j))^2+(pos_Fe16(2,i)-
pos_Fe16(2,j))^2+(pos_Fe16(3,i)-pos_Fe16(3,j))^2);
      bond_18(i,j)=sqrt((pos_Fe18(1,i)-pos_Fe18(1,j))^2+(pos_Fe18(2,i)-
pos_Fe18(2,j))^2+(pos_Fe18(3,i)-pos_Fe18(3,j))^2);
      bond_20(i,j)=sqrt((pos_Fe20(1,i)-pos_Fe20(1,j))^2+(pos_Fe20(2,i)-
pos_Fe20(2,j))^2+(pos_Fe20(3,i)-pos_Fe20(3,j))^2);
      bond_24(i,j)=sqrt((pos_Fe24(1,i)-pos_Fe24(1,j))^2+(pos_Fe24(2,i)-
pos_Fe24(2,j))^2+(pos_Fe24(3,i)-pos_Fe24(3,j))^2);
      bond_30(i,j)=sqrt((pos_Fe30(1,i)-pos_Fe30(1,j))^2+(pos_Fe30(2,i)-
pos_Fe30(2,j))^2+(pos_Fe30(3,i)-pos_Fe30(3,j))^2);
      bond_36(i,j)=sqrt((pos_Fe36(1,i)-pos_Fe36(1,j))^2+(pos_Fe36(2,i)-
pos_Fe36(2,j))^2+(pos_Fe36(3,i)-pos_Fe36(3,j))^2);
      bond_42(i,j)=sqrt((pos_Fe42(1,i)-pos_Fe42(1,j))^2+(pos_Fe42(2,i)-
pos_Fe42(2,j))^2+(pos_Fe42(3,i)-pos_Fe42(3,j))^2);
   end
end
n_Fe_2=zeros(1,192);
n_Mg_2=zeros(1,192);
n_Fe_3=zeros(1,192);
n_Mg_3=zeros(1,192);
n_Fe_4=zeros(1,192);
n_Mg_4=zeros(1,192);
n_Fe_5=zeros(1,192);
n_Mg_5=zeros(1,192);
n_Fe_6=zeros(1,192);
n_Mg_6=zeros(1,192);
n_Fe_7=zeros(1,192);
n_Mg_7=zeros(1,192);
n_Fe_8=zeros(1,192);
```

```
n_Mg_8=zeros(1,192);
n_Fe_9=zeros(1,192);
n_Mg_9=zeros(1,192);
n_Fe_10=zeros(1,192);
n_Mg_10=zeros(1,192);
n_Fe_11=zeros(1,192);
n_Mg_11=zeros(1,192);
n_Fe_12=zeros(1,192);
n_Mg_12=zeros(1,192);
n_Fe_13=zeros(1,192);
n_Mg_13=zeros(1,192);
n_Fe_14=zeros(1,192);
n_Mg_14=zeros(1,192);
n_Fe_16=zeros(1,192);
n_Mg_16=zeros(1,192);
n_Fe_18=zeros(1,192);
n_Mg_18=zeros(1,192);
n_Fe_20=zeros(1,192);
n_Mg_20=zeros(1,192);
n_Fe_24=zeros(1,192);
n_Mg_24=zeros(1,192);
n_Fe_30=zeros(1,192);
n_Mg_30=zeros(1,192);
n_Fe_36=zeros(1,192);
n_Mg_36=zeros(1,192);
n_Fe_42=zeros(1,192);
n_Mg_42=zeros(1,192);
for i=1:192
   for j=1:192
      if  bond_2(i,j) <= 12
```

```
    if j <= 8
        n_Fe_2(i)=n_Fe_2(i)+1;
    else
        n_Mg_2(i)=n_Mg_2(i)+1;
    end
end
if  bond_3(i,j) <= 12
    if j <= 12
        n_Fe_3(i)=n_Fe_3(i)+1;
    else
        n_Mg_3(i)=n_Mg_3(i)+1;
    end
end
if  bond_4(i,j) <= 12
    if j <= 16
        n_Fe_4(i)=n_Fe_4(i)+1;
    else
        n_Mg_4(i)=n_Mg_4(i)+1;
    end
end
if  bond_5(i,j) <= 12
    if j <= 20
        n_Fe_5(i)=n_Fe_5(i)+1;
    else
        n_Mg_5(i)=n_Mg_5(i)+1;
    end
end
if  bond_6(i,j) <= 12
    if j <= 24
        n_Fe_6(i)=n_Fe_6(i)+1;
```

```
    else
        n_Mg_6(i)=n_Mg_6(i)+1;
    end
end
if  bond_7(i,j) <= 12
    if j <= 28
        n_Fe_7(i)=n_Fe_7(i)+1;
    else
        n_Mg_7(i)=n_Mg_7(i)+1;
    end
end
if  bond_8(i,j) <= 12
    if j <= 32
        n_Fe_8(i)=n_Fe_8(i)+1;
    else
        n_Mg_8(i)=n_Mg_8(i)+1;
    end
end
if  bond_9(i,j) <= 12
    if j <= 36
        n_Fe_9(i)=n_Fe_9(i)+1;
    else
        n_Mg_9(i)=n_Mg_9(i)+1;
    end
end
if  bond_10(i,j) <= 12
    if j <= 40
        n_Fe_10(i)=n_Fe_10(i)+1;
    else
        n_Mg_10(i)=n_Mg_10(i)+1;
```

```
    end
end
if  bond_11(i,j) <= 12
    if j <= 44
        n_Fe_11(i)=n_Fe_11(i)+1;
    else
        n_Mg_11(i)=n_Mg_11(i)+1;
    end
end
if  bond_12(i,j) <= 12
    if j <= 48
        n_Fe_12(i)=n_Fe_12(i)+1;
    else
        n_Mg_12(i)=n_Mg_12(i)+1;
    end
end
if  bond_13(i,j) <= 12
    if j <= 52
        n_Fe_13(i)=n_Fe_13(i)+1;
    else
        n_Mg_13(i)=n_Mg_13(i)+1;
    end
end
if  bond_14(i,j) <= 12
    if j <= 56
        n_Fe_14(i)=n_Fe_14(i)+1;
    else
        n_Mg_14(i)=n_Mg_14(i)+1;
    end
end
```

```
if  bond_16(i,j) <= 12
   if j <= 64
      n_Fe_16(i)=n_Fe_16(i)+1;
   else
      n_Mg_16(i)=n_Mg_16(i)+1;
   end
end
if  bond_18(i,j) <= 12
   if j <= 72
      n_Fe_18(i)=n_Fe_18(i)+1;
   else
      n_Mg_18(i)=n_Mg_18(i)+1;
   end
end
if  bond_20(i,j) <= 12
   if j <= 80
      n_Fe_20(i)=n_Fe_20(i)+1;
   else
      n_Mg_20(i)=n_Mg_20(i)+1;
   end
end
if  bond_24(i,j) <= 12
   if j <= 96
      n_Fe_24(i)=n_Fe_24(i)+1;
   else
      n_Mg_24(i)=n_Mg_24(i)+1;
   end
end

if  bond_30(i,j) <= 12
```

```
        if j <= 120
            n_Fe_30(i)=n_Fe_30(i)+1;
        else
            n_Mg_30(i)=n_Mg_30(i)+1;
        end
    end

    if  bond_36(i,j) <= 12
        if j <= 144
            n_Fe_36(i)=n_Fe_36(i)+1;
        else
            n_Mg_36(i)=n_Mg_36(i)+1;
        end
    end

    if  bond_42(i,j) <= 12
        if j <= 168
            n_Fe_42(i)=n_Fe_42(i)+1;
        else
            n_Mg_42(i)=n_Mg_42(i)+1;
        end
    end
  end
end
avg_Fe_Fe2=sum(n_Fe_2(1:8))/8;
avg_Fe_Fe3=sum(n_Fe_3(1:12))/12;
avg_Fe_Fe4=sum(n_Fe_4(1:16))/16;
avg_Fe_Fe5=sum(n_Fe_5(1:20))/20;
avg_Fe_Fe6=sum(n_Fe_6(1:24))/24;
avg_Fe_Fe7=sum(n_Fe_7(1:28))/28;
```

```
avg_Fe_Fe8=sum(n_Fe_8(1:32))/32;
avg_Fe_Fe9=sum(n_Fe_9(1:36))/36;
avg_Fe_Fe10=sum(n_Fe_10(1:40))/40;
avg_Fe_Fe11=sum(n_Fe_11(1:44))/44;
avg_Fe_Fe12=sum(n_Fe_12(1:48))/48;
avg_Fe_Fe13=sum(n_Fe_13(1:52))/52;
avg_Fe_Fe14=sum(n_Fe_14(1:56))/56;
avg_Fe_Fe16=sum(n_Fe_16(1:64))/64;
avg_Fe_Fe18=sum(n_Fe_18(1:72))/72;
avg_Fe_Fe20=sum(n_Fe_20(1:80))/80;
avg_Fe_Fe24=sum(n_Fe_24(1:96))/96;
avg_Fe_Fe30=sum(n_Fe_30(1:120))/120;
avg_Fe_Fe36=sum(n_Fe_36(1:144))/144;
avg_Fe_Fe42=sum(n_Fe_42(1:168))/168;

figure(1)
plot([8*100/192,12*100/192,16*100/192,20*100/192,24*100/192,28*100/192,32*100/192,36*100/
192,40*100/192,44*100/192,48*100/192,56*100/192,64*100/192,72*100/192,80*100/192,96*100/
192,120*100/192,144*100/192,168*100/192],[avg_Fe_Fe2,avg_Fe_Fe3,avg_Fe_Fe4,avg_Fe_Fe5,avg_
Fe_Fe6,avg_Fe_Fe7,avg_Fe_Fe8,avg_Fe_Fe9,avg_Fe_Fe10,avg_Fe_Fe11,avg_Fe_Fe12,avg_Fe_Fe14,av
g_Fe_Fe16,avg_Fe_Fe18,avg_Fe_Fe20,avg_Fe_Fe24,avg_Fe_Fe30,avg_Fe_Fe36,avg_Fe_Fe42],'k--*')
xlabel('Fe Concentration [%]')
ylabel('Number of Fe Neighbours')
```